Pulse Shape Discrimination Studies in Liquid Argon for the DEAP-1 Detector

By

Jeffrey Jack Lidgard

A thesis submitted to the Department of Physics, Engineering Physics

and Astronomy in conformity with the requirements for the degree of Master of Science

Queen's University

Kingston, Ontario, Canada

April, 2008

Abstract

A detector with a target mass of 7 kg of liquid argon was designed, constructed and operated at Queen's University. This detector is a scaled model for the DEAP project toward a tonne-scale argon detector to search for the WIMP candidate of the so far undetected, dark matter of the universe. The primary intent of the scaled detector was to measure the achievable level to reject background events by use of pulse shape discrimination, being based upon the scintillation timing properties of liquid argon. After refining the apparatus and components, the detector was in operation from the 20th of August until the 16th of October 2007 before being moved to its current location in SNOLAB. During this time, a population of 31 million well-tagged gamma events were collected, of which 15.8 million were in the energy range of interest for calibration. This population was sufficient to demonstrate the discrimination of background events by pulse shape discrimination at the level of 6.3×10^{-8}. An analytical model was constructed, based on the scintillation processes and detector response, and has been sufficiently investigated to make predictions of further achievable discrimination.

Acknowledgements

Firstly, I would like to thank Dr Mark Boulay whom I am proud to have had as a mentor and supervisor, whose ideas have made such work possible and whose guidance and support has helped me to produce this thesis. There are, however, many others at Queen's who have made such work possible: the professors and staff throughout the physics department and those with whom I have worked closely and whose help and time I am grateful for, Bei Cai, Mark Chen, Kevin Graham (Carleton University), Chris Jillings (SNOLAB), Paradorn Pasuthip, Wolfgang Rau, Peter Skensved and David Bearse, Chuck Hearns, Rob Gagnon and all the summer students who have been so helpful. My fellow students, who have not only been a wealth of knowledge but have also, along with those already mentioned, made my time here enjoyable: Mark Kos, John Golightly, Ryan MacLellan, Ryan Martin, Sarah Quirk, Alex Wright, as well my loving girlfriend, my friends and family, whose patience and support I could not have done without.

Contents

List of Figures

List of Tables

Chapter 1

Introduction

1.1 Premise for Dark Matter

The observational evidence for the existence of a non-luminous portion of matter present in galaxies is now well established and is observed to make up a large fraction of the mass in the universe, many times the mass of ordinary matter. A discovery in the composition would lead to an increased understanding of the dark fraction and of the grand structure of our universe.

The universe is known to be expanding according to Hubble's law, measured at a rate of 72 ± 8 km/s/Mpc [1]. The space-time geometry of the universe is currently believed to be flat, and given by the Friedmann-Lemaître-Robertson-Walker (FLRW) model, with an energy density so that,

$$\Omega = \frac{\rho}{\rho_c} \simeq 1 \qquad (1.1)$$

where ρ_c is the critical density required for a flat universe, described by Euclidean space and Ω is a factor representing the average energy density of the universe. The other possible cases are where $\Omega < 1$, for which the space-time of the universe has a negative curvature and would expand forever, and $\Omega > 1$, for positive curvature, leading to a re-collapse. Measurements of the cosmic microwave background, made very accurately by WMAP, measure Ω to be 1.02 ± 0.02 [2]. Of this energy density, the contribution of baryonic matter has been measured, also by WMAP, to be 4% of the total mass [2]. Radiation, including neutrinos, contributes no significant portion. Of the remaining fraction, 24% [2] is believed to be cold dark matter, responsible for gravitational effects seen in the structure of matter, and 73% [2] is some form of exotic energy, named dark energy, contributing the required energy for the observed Ω, similar in nature to some cosmological constant.

1.2 Observational Evidence for Dark Matter

The dark matter component of the universe has been observed at several length scales. Early evidence for dark matter was obtained by Fritz Zwicky, in 1933 [3][4], while observing galaxies within the Coma cluster. When applying the measured orbits to the virial theorem, Zwicky noted a much larger mass than that which could be observed was required for the observed orbits.

On the scale of galaxies, evidence can be obtained from a galaxies velocity dispersion curve, where the orbital rotational speed, inferred from measurements of their Doppler shift, is plotted as a function of distance from the galaxies centre. The observation of increased orbital speeds at large distances from the galactic centre indicates the presence of a mass significantly greater than the luminous matter observed. These curves are of the more common evidence and have been made for many galaxies. Early evidence for dark matter in galaxies was observed by Babcock in 1939 for the Andromeda galaxy, and Oort in 1940 studying NGC3115 [4].

Evidence has also been observed through the gravitational lensing of clusters. Gravitational lensing of cosmological objects is the bending effect of the light produced from a distance source as it passes a large body of mass. The mass distribution of dark matter in galaxies has been reported [5] by use of weak lensing, where the lensing produces subtle shape distorting effects and is studied statistically. A unique example of dark matter observed by weak gravitational lensing is observed in the Bullet cluster [6].

The foremost candidate particle has become known as the Weakly Interacting Massive Particle, or WIMP [6]. Of the observational evidence, basic assumptions can be made of the particle. The clumping of dark matter seen in matter structures requires that it be non-relativistic. The particle is to be of considerable mass, on the order of many times the mass of the proton (10-1000 GeV). Current searches place a limit on the cross-section for interaction of $4.6\text{x}10^{-44}\text{cm}^2$ for a 60 GeV WIMP made recently by the CDMS [7] collaboration and $4.5\text{x}10^{-44}$ cm^2 for a WIMP mass of 30 GeV by the Xenon collaboration [8].

Theories of supersymmetry predict a particle, the neutralino, with similar properties to WIMPs, results of which will be tested in new, high energy particle accelerators, namely the LHC, currently being constructed and nearing completion at CERN, and the future ILC.

1.3 Direct Detection

Detecting a particle interacting only via the weak force poses a considerable experimental difficulty, made known to the experimental community since the discovery of the neutrino in 1956, now thoroughly explored and overcome by neutrino experiments such as the Sudbury Neutrino Observatory (SNO) [10][11], Super-Kamiokande [12] and KamLAND [13]. SNO detects Cherenkov radiation produced by electrons as a product of an inverse beta decay initiated by an incident neutrino. KamLAND detects the scintillation produced by the elastic scattering of neutrinos with electrons, situated to utilise the large flux of neutrinos produced by nuclear reactors.

In detecting the WIMP, the mass of the proposed particle is sufficient to produce detectable recoil of nuclei in an elastic collision.

$$\chi + Ar \rightarrow \chi' + Ar' \tag{1.2}$$

The energy of the recoiling nucleus, E_r, is given by kinematics,

$$E_r = \frac{m_N m_\chi}{\left(m_N + m_\chi\right)^2} m_\chi v^2 \left(1 - \cos\theta\right) \tag{1.3}$$

where m_N is the mass of the target nuclei and m_χ the mass of the WIMP, v is the relative speed, and θ is the centre of mass scattering angle. The particles are expected to be in orbit around the centre of the galaxy with a Maxwellian distribution of speeds, with an average speed of 270 ± 50 km/s [14] (~0.001 c). The recoil energy spectrum is heavily dependent on the choice of target, dependent on both the number of nucleons and form factor. Hence, for an argon nucleus, we expect nuclear recoils of energies on the order of tens of keV. Thus a detector with a low energy threshold is required.

The rate within the detector will be dependent on the flux of WIMPs through the Earth. The dark matter halo is assumed to be spherically symmetric with density given by,

$$\rho(r) = \rho_0 \frac{r_c^{\,2}}{r^2 + r_c^{\,2}} \tag{1.4}$$

where r is the radial distance, r_c is the radius of the halo core (~56 kpc) and ρ_0 the central core density (~1.0 Gev/cm^3). These assumptions lead to an approximate flux on the order of 10^5 /s/cm^2 [15] for 1GeV WIMPs on Earth. Given the current limit on the WIMP cross-section, the expected event count rate is on the order of a few counts/kg/year.

The cross-section for interaction is dependent on the spin properties of the WIMP. It is currently favoured for the WIMP to have zero spin. If the WIMP has spin, only nuclei with spin will have a sufficient interaction cross-section to detect experimentally, making the choice of an experimental target even more ambiguous. Depending on the choice of target, a detector can be categorised a spin-dependent or spin-independent detector, though spin-dependent detectors have some sensitivity to the zero spin interaction. There are many suitable targets for spin-independent searches and only few for spin-dependent searches. Comparatively, the spin-independent detectors have currently reached a higher level of sensitivity, discussed in section 1.5.

A detector with a threshold low enough to detect the elastic scattering of WIMPs will also have a high rate of background events from terrestrial sources interacting in the detector. Therefore a sufficient method is required to differentiate nuclear recoil events, from electronic recoil produced by gamma and beta radiation depositing energy within the detector.

1.4 DEAP

1.4.1 Introduction & Aim

The experiment within the focus of this thesis, DEAP (Dark matter Experiment using Argon Pulse shape discrimination), utilises a mass of liquid argon as a WIMP target.

To develop an evolution of the technology, the project was portioned into three segments. DEAP-0 was a prototype detector in which the scintillation properties of argon were investigated [16]. DEAP-1 (10^1 kg target) is the precursor to the larger DEAP-3 (10^3 kg target).

The aim of DEAP-1 is to demonstrate the required pulse shape discrimination, while also quantifying some of the yet unmeasured characteristics of liquid argon, to study backgrounds and to further refine cryogenic procedures to ease the engineering and construction to scale the target mass to the larger DEAP-3.

1.4.2 Background & History

Pioneering work toward the use of argon as a dark matter target was completed at Los Alamos National Laboratory in 2004-2005 [16]. Here the initial investigation of pulse shape discrimination in argon was completed in an experiment named DEAP-0.

During 2005 work began toward the construction of DEAP-1 at Queen's University. In the following years the system developed into a working, efficient detector through the ongoing construction and refining of the apparatus. The last quarter of 2007 was spent in the deployment of the detector at the underground experimental site in SNOLAB, [17] 6800 feet below surface in the INCO owned nickel mine in Sudbury, Ontario.

1.4.3 Status

DEAP-1 is currently in operation within SNOLAB. Data towards a dark matter search is being collected, while the system is being further refined to enhance its sensitivity. Investigation in the use of a nitrogen purged atmosphere to reduce the background due to radon contamination is underway.

1.4.4 Collaboration

The collaboration and history of the experiment has produced a collaboration collectively working together, simultaneously on respective areas of the DEAP and CLEAN experiments, and come to be known as the DEAP/CLEAN collaboration. The aim of the collaboration is to aid the development of both projects, which share similar technology and methods, as both experiments are large-mass, low threshold, cryogenic noble liquid scintillation detectors.

Currently there are members working towards DEAP at Queen's University (Dr. Mark Boulay, Dr. Mark Chen, Dr. Arthur McDonald), Carleton University (Dr. Kevin Graham), University of Alberta (Dr. Aksel Hallin) Yale University (Dr. Daniel McKinsey), Los Alamos National Laboratory (Dr. Andrew Hime), SNOLAB (Dr. Bruce Cleveland, Dr. Fraser Duncan, Dr. Chris Jillings, Dr Ian Lawson,), Boston University (Dr. Edward Kerns), the University of Texas at Austin (Dr. Josh Klein).

1.5 Current Searches and Limits

While there are several very good, sophisticated experiments in operation and on the horizon, only a select few are outlined here in order to give an instructive introduction to the technology.

1.5.1.1 CDMS

The Cryogenic Dark Matter Search (CDMS) has been in operation underground in the Soudan mine in Minnesota since 2003. CDMS measures the charge and phonons generated from an ionization event in ultra-pure crystals of silicon and germanium. The charge and phonon measurements are made simultaneously for each interaction. The charge is drifted out of the crystals by an applied electric field, while the phonon signal is inferred from the deviation of temperature of the semiconductor crystals from their milli-Kelvin operating temperature. In germanium, charge pairs are created by 3 eV of energy; thus the bias is tuned to drift the charge out, without significantly affecting the signal and the signal is collected at multiple sites over the crystal. The detector response, in number of ionization pairs and number of phonons, is calibrated to equate the number of phonons to charge. Nuclear recoil events produce ionization of charge and phonons in a different ratio to electronic recoils, and as such the different events can be identified. Currently CDMS utilises stacks of 250 g germanium crystals or 100 g silicon crystals, 1 cm thick, 7.8 cm in diameter, while adding new stacks to increase the sensitive mass. The production of these detectors however is prohibitively expensive in scaling the experiment to larger mass scales. The experiment has so far published 480 kg-years of data and has published a limit on the spin-independent cross-section of 4.6×10^{-44} cm^2 for a WIMP mass of 60 GeV [8].

1.5.1.2 Xenon

The Xenon experiment utilises a mass of liquid xenon as a dark matter target. Xenon scintillates in the manner similar to other noble materials, though with different timing characteristics. In addition to collecting scintillation light, ionization charge is drifted through the xenon mass by an applied electric field. Nuclear recoil events are differentiated from electronic recoil by use of the relative amounts of light and charge collected. The timing characteristics of the scintillation light produced by xenon have a very short decay time compared to that of other noble liquids, and thus background rejection achievable by pulse shape discrimination alone is decreased. Xenon has the advantage of having a very large atomic number though suffers from relatively small form factor. Being a liquid target, it is relatively easy to scale to larger masses, though xenon is the most expensive of the noble gases.

Xenon-10, an experiment utilising a mass of 15 kg (5.4 kg fiducial) of xenon has been in operation underground in Gran Sasso National Laboratory in Italy. With this detector 16.8 days (livetime) of data were collected in 2006. The collaboration has recently published a limit on the spin-independent cross-section of 4.5×10^{-44} cm^2 for a WIMP mass of 30 GeV [9]. The construction of a 100 kg detector is underway.

1.5.1.3 Picasso

The Picasso (Project In Canada to Search for Super-symmetric Objects) detects the vibration generated when a WIMP interaction induces a phase transition of superheated droplets of Freon, based on bubble chamber technology. The detector utilises a mass of Freon (C_4F_{10}), since ^{19}F is one of the more favourable nuclei for a spin-dependent search, largely due to its increased form factor. The droplets have an average diameter of 11 micrometers and are suspended within a gel. The energy required for a phase transition for one of the droplets is dependent on the operating temperature and pressure. The sensitivity to neutron, alpha and gamma radiation is dependent on these operating parameters.

The first stage of Picasso, deployed in SNOLAB, consisted of 3 detector modules each containing 1.0 litre of 0.5% Freon loaded gel, and has published a limit on the spin-dependent cross-section of 21.5 pico-barns (2.15×10^{-35} cm^2) for neutrons and 1.31 pico-barns (1.31×10^{-36} cm^2) for protons [18][19]. The next stage is currently underway with an increased number of upgraded detectors, each with higher Freon loading.

1.5.1.4 CLEAN

CLEAN (Cryogenic Low Energy Astrophysics with Noble gases) utilises a mass of liquid argon for a WIMP sensitive search, with the ability to use liquid neon for a precise measurement of the *pp* solar neutrino flux, and scalable to 10 tonnes for a dark matter search with liquid neon. Neon scintillates, similarly to other noble gases, though has a longer triplet lifetime and thus enhanced PSD. However, neon is one of the lighter noble gases and thus requires such a large mass for a sensitive dark matter search. The design and experimental basis are similar to those used in DEAP [20] though the engineering differs, mainly due to the increased size and lower liquefaction temperature for neon at 27 Kelvin, compared to argon at 87 Kelvin. The first stage of the CLEAN project, microCLEAN, with a 4 kg mass of liquid argon is underway at Yale University [21][22]. A larger detector with a mass of 360 kg is currently under development and is to be deployed in SNOLAB.

Chapter 2

Searching for Dark Matter with Argon

2.1 Scintillation in Liquid Argon

In noble liquids, scintillation light is produced typically in the high UV by the de-excitation of dimer states. An incident particle, upon interacting and depositing energy within the liquid, will lead to the production of dimer states and the production of scintillation.

In terms of a dark matter target, the possibility for tonne-scale masses and the ease of purification make noble liquids highly desirable. The scalability of noble liquid detectors has made them an asset for many large scale radiation detectors, for example in particle tracking for large particle physics experiments [23].

This chapter concerns the scintillation and other basic properties of argon, the noble liquid target utilised in DEAP, and similarly in the WARP dark matter detector [24]. The other noble elements have similar scintillation properties, in particular neon and xenon, which are currently being investigated as targets in other dark matter searches [9][21]. Krypton and radon both have an internal radioactive component, larger than that of argon, and hence not of interest here. Helium is not a practical target for dark matter due to its low mass.

Most noble gases are sourced through the liquefaction of atmosphere. Neon and argon can be bought commercially at low cost making large targets feasible. However, xenon being less abundant, is more expensive. Noble gases have a liquefaction point at cryogenic temperatures, neon at 27 K, argon at 87 K, and xenon at 165 K, therefore a large mass requires some work to produce and maintain.

2.1.1 Excitation Processes

An incident particle interacting in the target noble liquid will both ionize and excite atoms. These atoms quickly form dimer states. The ionized state can undergo recombination with electrons to produce a dimer. Of the dimers in argon, three spin states are possible, two singlets, of which one cannot decay radiatively by parity conservation, and a triplet [25]. The ratio of the produced states is dependent on the incident particle. These states, being populated only after a deposition of energy, are unstable and free to decay, which quickly do so by emission of a photon. In argon this scintillation is peaked at 128 nm, in neon at 77 nm, and xenon at 175 nm.

The scintillation yield of noble liquids is on the order of tens of thousands of photons per MeV, comparable to common inorganic scintillators, such as NaI. The population of dimers produced, and therefore light yield, is dependent on the source of excitation. Numbers in literature are fairly variable, possibly due to being dependent on geometry, temperature and some absolute quantities being converted from a relative yield to helium. Table 2.1 summarises values for electron events.

	Scintillation Yield
Neon	15000 photons/MeV[27]
Argon	40000 photons/MeV[28]
Xenon	42000 photons/MeV[28]
NaI	43000 photons/MeV[28]

Table 2.1: Scintillation yields for electron excitation.

2.1.2 Timing Characteristics

As an incident particle will produce both singlets and triplet dimers, the scintillation is a product of the two radiative decays. The singlet decays quickly, responsible for most of the prompt light seen in the scintillation spectrum, whereas the triplet decays with a longer lifetime. The time constant of the singlet and triplet decays have been measured in all phases for most noble gases, summarised in Table 2.2 for liquid Ne, Ar, Xe.

	Singlet Lifetime (ns)	Triplet Lifetime (ns)
Neon[a]	18.2 ± 0.2	14900 ± 300
Argon[b]	7.0 ± 1.0	1600 ± 100
Xenon[b]	4.3 ± 0.6	22.0 ± 2.0

Table 2.2: Singlet and triplet time constants in noble liquids
(a taken from [21][22], b from [29])

The population of the particular dimer produced is dependent on the charge density of the incident particle. For nuclear recoil events, a larger singlet to triplet ratio is observed than for electronic excitation, summarised in Table 2.3.

	Singlet / Triplet (I_s/I_T)		
	Electrons	Alphas	Fission Fragments
Neon_a	2.0	8.7	20
Argon_b	0.3	1.3	3.0
Xenon_b	0.05	0.45 ± 0.07	1.6 ± 0.2

Table 2.3: Singlet to triplet ratio in noble liquids
(a taken from [20], b from [29])

Quenching of the singlet and triplet states can occur, effectively reducing the photon yield. Scintillation produced for nuclear recoils is greatly affected, due to the increased density of excitation, leading to an increased probability for these states to self-interact and de-excite in a non-radiative manner. As such, the factors quoted are typically relative to the photon yield produced for electron recoil.

Literature values for quenching factors are quite variable. The quenching in argon has been reported for nuclear recoils to be 0.26 – 0.3 [24][31]. For comparison, quenching in neon has been measured to be 0.26 ± 0.03 [22] for 387 keV nuclear recoils and in xenon [31] to be 0.13 at 10.3 keV up to 0.23 at 56 keV.

Further destruction of triplet states can occur by non-radiative interactions with impurities. It has been reported for gaseous argon [25], very small quantities of impurities can significantly decrease the observed lifetime due to the destruction of triplets.

The decay times along with the singlet to triplet ratio and quenching factors, determine the scintillation time structure, indicated in Figure 2.1.

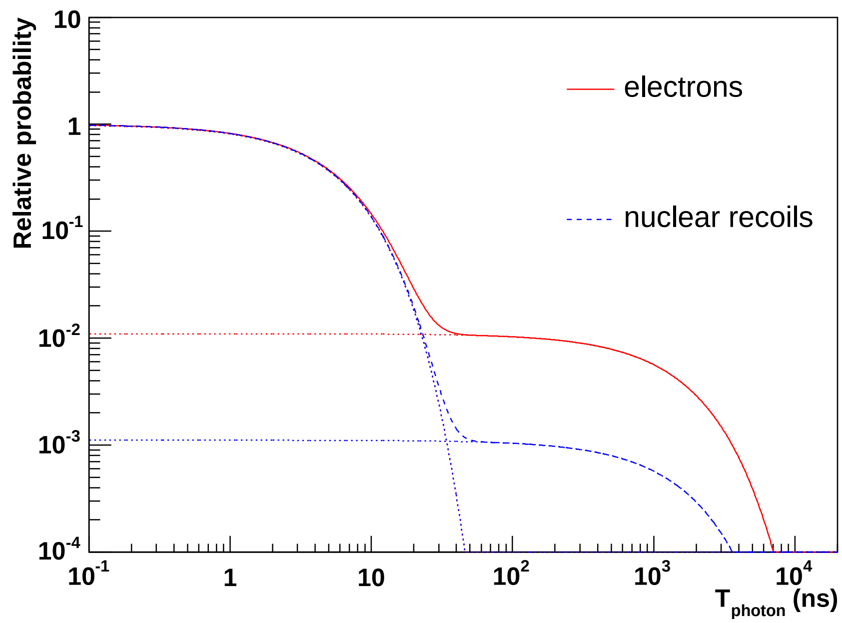

Figure 2.1 Scintillation time distribution produced from dimer states in argon

2.1.3 Photon Absorption

Impurities in commercial argon must be removed as they can absorb scintillation light, reducing the total light yield. Also, impurities would increase the rate of non-radiative transitions in the de-excitation of the dimers, particularly the triplet, as discussed in 2.1.1. The argon gas is purified with a SAES getter, discussed in 3.1.1, which reduces common impurities to less than 1 ppb [32].

Argon does not absorb its scintillation light; hence, in the absence of impurities the optical path length is long. In Monte Carlo studies of a detector 3 m in radius filled with neon, it was found an absorption length of approximately 300 m was required to attain 95% of light [20]. Neon has similar properties to argon, and a shorter Rayleigh scattering length, shown in Table 2.4. Here we estimate the path length in argon is at least 2.8 m, a value 10 times longer than the detector length.

	Scattering Length (cm)
Neon	60
Argon	90
Xenon	30

Table 2.4: Rayleigh scattering lengths in noble liquids [33]

We calculate the tolerable concentration of common impurities for photons of this path length. A similar method to the one used here was used for liquid neon [20]; using cross-sections complied by Gallagher [34]. The transmission is defined by the Beer-Lambert law as,

$$T = \frac{I_1}{I_0} = e^{-\alpha(\lambda)x} \tag{2.1}$$

where x is the distance over which the absorption takes place and $\alpha(\lambda)$ is the absorption coefficient at wavelength λ.

The absorption coefficient for N absorbers is given by,

$$\alpha = \frac{1}{l} = \sum_{i=1}^{N} \frac{\rho N_A \gamma_i \sigma_i}{M_i} \tag{2.2}$$

where

- l is the mean free path of the photons, here 2.8 m.
- ρ is the density of the medium, here for argon equal to 1430 kg/m^3.
- N_A is Avogadro's number (6.022×10^{23} particles/mole),

- γ_i is the mass fraction of the absorber,
- σ is the photo-absorption cross-section of the impurity at wavelength λ,
- M_i is the molar mass of the absorber.

We assume the absorption is equally divided for the N absorbers; as in [20], we set the tolerable mass fraction of impurities to be,

$$\gamma_i = \frac{M_i}{N \rho N_A \sigma_i l} \tag{2.3}$$

As it is possible to purify argon to impurities on the order of ppb, we seek cross-sections for the molecular absorption of light. However data on the molecular absorption for simple compounds is sparse. The cross-sections complied by Gallagher do not extend beyond 100 nm. Here we calculate an upper limit for the concentrations for an impurity concentration of 1 ppb, summarised in Table 2.5.

Impurity	Concentration (ppb)	Cross-section Limit for 1 ppb concentration (cm^2)
H_2	1	2.1×10^{-18}
H_2O	1	1.9×10^{-17}
N_2	1	2.9×10^{-17}
O_2	1	3.3×10^{-17}

Table 2.5 Impurity absorption cross-sections and impurity limits

These cross-sections are larger than those reported for the absorbance of the 80 nm light of neon, which are observed to decrease beyond 100 nm; hence the cross-sections for the absorbance of 128 nm photons are expected to be even smaller than those at 80 nm. This implies the impurities are more likely to quench the triplet states, as was found by [25], rather than absorb scintillation photons.

2.2 Backgrounds in DEAP-1

In this section we describe the sources of background radiation capable of producing scintillation events, both intrinsic to the detector and from external sources. These include internal beta events from the decay of argon-39, neutron and alpha backgrounds from detector material impurities, and finally external backgrounds from cosmic rays.

2.2.1 Argon-39

One of the radioisotopes of argon, ^{39}Ar, is naturally abundant in the atmosphere, being produced by cosmic rays, as in equation (2.4). Argon-39 decays by emission of a beta particle with end point energy of 0.565 MeV and half life of 269 years.

$$\begin{aligned} &^{40}Ar + n \rightarrow {}^{39}Ar + 2n \\ &\qquad\qquad\quad \searrow \\ &\qquad\qquad\qquad {}^{39}Ar \rightarrow {}^{39}K + \beta^- + \overline{\upsilon} \end{aligned} \tag{2.4}$$

The mass fraction of argon-39 has been measured to be $(7.9 \pm 0.3) \times 10^{-16}$ gram /gram [36] of natural argon. As commercial argon is sourced from the liquefaction of atmosphere, ^{39}Ar is expected to be present in the same fraction. The specific activity of argon-39 is measured to be 1.01 ± 0.02 (stat) ± 0.08 (syst) Bq/kg [37] of natural argon.

The beta spectrum in units of decays of argon-39 per kg per year is shown in Figure 2.2.

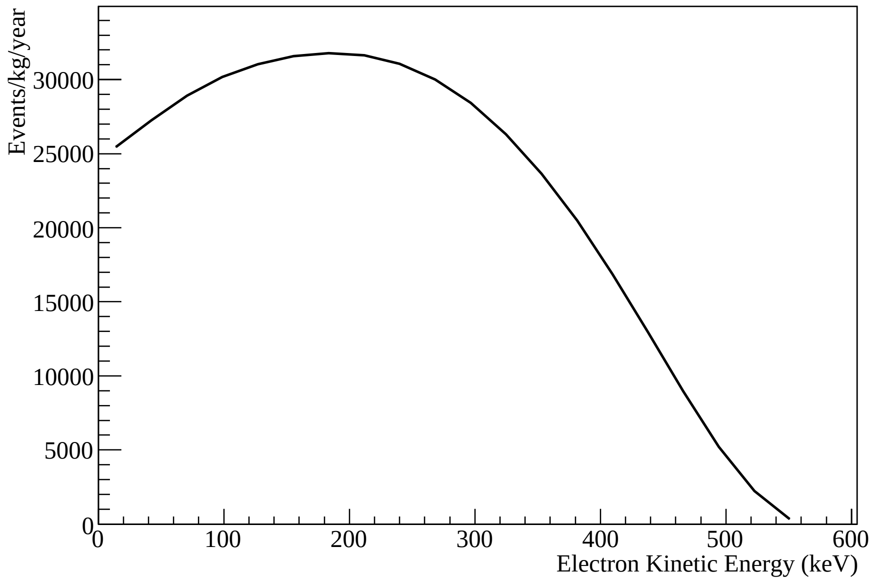

Figure 2.2: Beta spectrum of argon-39
(calculated by [39])

For the energy region of interest for a WIMP search we seek recoil energies of 60 – 120 keV, as given by equation (1.3). After quenching, this is approximately 20 – 40 keV. Integrating the beta spectrum over these energies we expect 5.5×10^5 events/kg/year. For 7 kg, as used in DEAP-1, this corresponds to 3.9×10^6 events/kg/year within the energy region of interest.

Being almost exclusively cosmogenically produced, it is possible to find sources of argon with a reduced fraction of argon-39 underground, for example in well gas [35], or in large storage facilities, such as the US National Helium Reserve, where the fraction of argon-39 has been measured to be 5% lower than in atmospheric argon [38]. Small contributions of argon-39 will be produced by beta and muon capture of potassium-39, though this is expected to be small [35]. A source of depleted argon would reduce the background rate and is being investigated.

2.2.2 Terrestrial Sources

In this section we consider the possibility that the materials used in construction are a source of background radiation due to radioactive impurities, and we estimate the number of events which could be generated.

In designing the detector, construction materials were selected while keeping in mind the need to minimise background radiation. Reliability and strength call for metals, though most metals contain a small percentage of the radioactive elements uranium and thorium or those within their decay chains. Acrylic is known to contain very low levels of radioactive impurities and is used where possible for both light transport and in construction in place of metal.

2.2.2.1 Material Impurities

The active argon region and photomultipliers are the more susceptible components to background radiation, though care was taken in the construction of the detector as a whole. The detector components are described in section 3.1. Stainless steel has a relatively lower activity than steel and was primarily used. The argon vessel is made of stainless steel. Acrylic is known to be relatively pure, containing very low concentrations of radio-impurities, used extensively by the SNO collaboration [40] and is used here where possible. For example, acrylic is used to house a vacuum around the inner chamber and as a light guide to the photomultipliers. The materials used and their radioactivity are summarised in Table 2.6 and Table 2.7.

Chain	Specific activity (Bq/g)	Total mass (g)
U	178.9×10^3 [20]	0.1223
Th	39.14×10^3 [20]	0.0771
K	30.30 [20]	50.197

Table 2.6: Total mass of radio-impurities in materials

Component	Material	Mass (kg)	U (ppb)	Th (ppb)	K (ppm)
Chamber	Stainless steel	40	0.511	1.90	0.2177
PMTs	Mixed	0.420	28	31	60
Dark box	Aluminium	46.6	1549.85	580.27	2.956
Shield stand	Mild Steel	500	100	100	100

Table 2.7: Radioactive impurities of uranium, thorium and potassium [41]

The expected number of neutrons produced by the decay alphas of the uranium and thorium impurities on detector material, (α,n) reactions, computed from Monte Carlo [33], are shown in Table 2.8.

The aluminium dark box is of concern as no shielding material is between this material and the detector. This material will be replaced with a more radio-pure material such as stainless steel, once the backgrounds presented by argon 39 and radon are reduced. The material for the shield stand is enclosed within the water shield, discussed in section 3.1.10.

Component	Material	n/year/kg/ppb (U)	n/year/kg/ppb (Th)	neutrons/year
Chamber	Stainless steel	0.124	0.138	13
PMTs	Mixed	10.53	0.138	126
Dark box	Aluminium	5.053	2.549	4.3×10^5
Shield stand	Mild Steel	0.124	9.6	4.9×10^5

Table 2.8: Expected neutron events per year from U & Th impurities [33]

2.2.2.2 Radon

Small amounts of the long-lived radioisotopes within the thorium-232 and uranium-238 decay chains are present in the atmosphere. These decay to produce the isotopes of radon, radon-222 (with half life of 3.8 days), and radon-224 (with half life of 3.6 days) respectively. A significant amount of radon is present in the atmosphere, and is responsible for most of the radioactive component of air.

Radon is problematic as the alphas produced in the decay chain will produce nuclear recoil scintillation events. The problem posed by radon here concerns the embedding of the decay daughters into the detector materials during construction. Here we describe in detail the decay of radon-222 within the U-238 chain, and is shown schematically in Figure 2.3. The alphas produced in the Th-232 decay chain are of equal concern, shown in Figure 2.4.

Radon-222 decays to polonium-218 which can electrostatically adhere to surfaces. Polonium-218 quickly decays through to lead-210, which when present on a surface, the decay can embed the lead-210 a short distance into the material, and with a half life of 22 years remains in the material for some time. Lead-210 decays to produce polonium-210 which alpha decays, presenting a long-lived source for (α, n) reactions. The neutrons are capable of producing neutron-like nuclear recoil events. Hence, radon daughters adhering to the surfaces of the argon vessel and windows are of concern. Care can be taken during construction to avoid the additional background due to radon contamination, by first sanding the possible contaminated surfaces and working in a reduced radon atmosphere by purging with clean boil-off gas of liquid nitrogen.

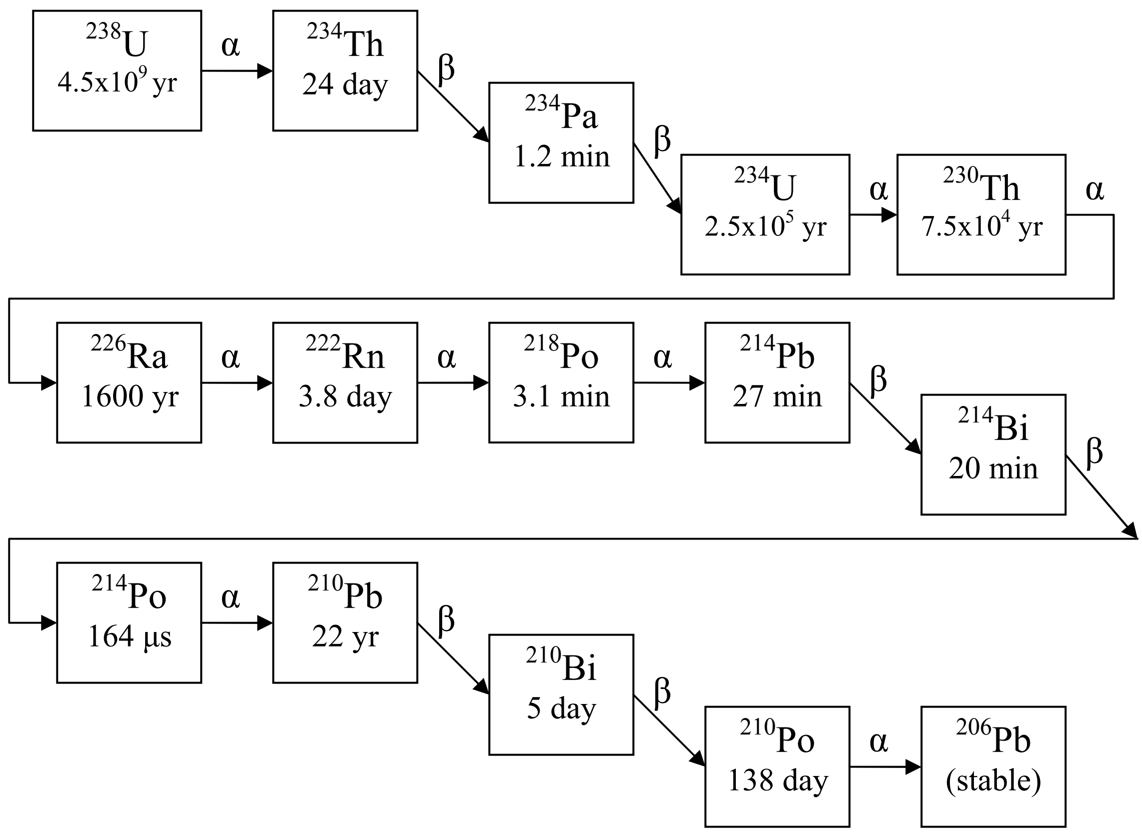

Figure 2.3: Uranium-238 decay chain

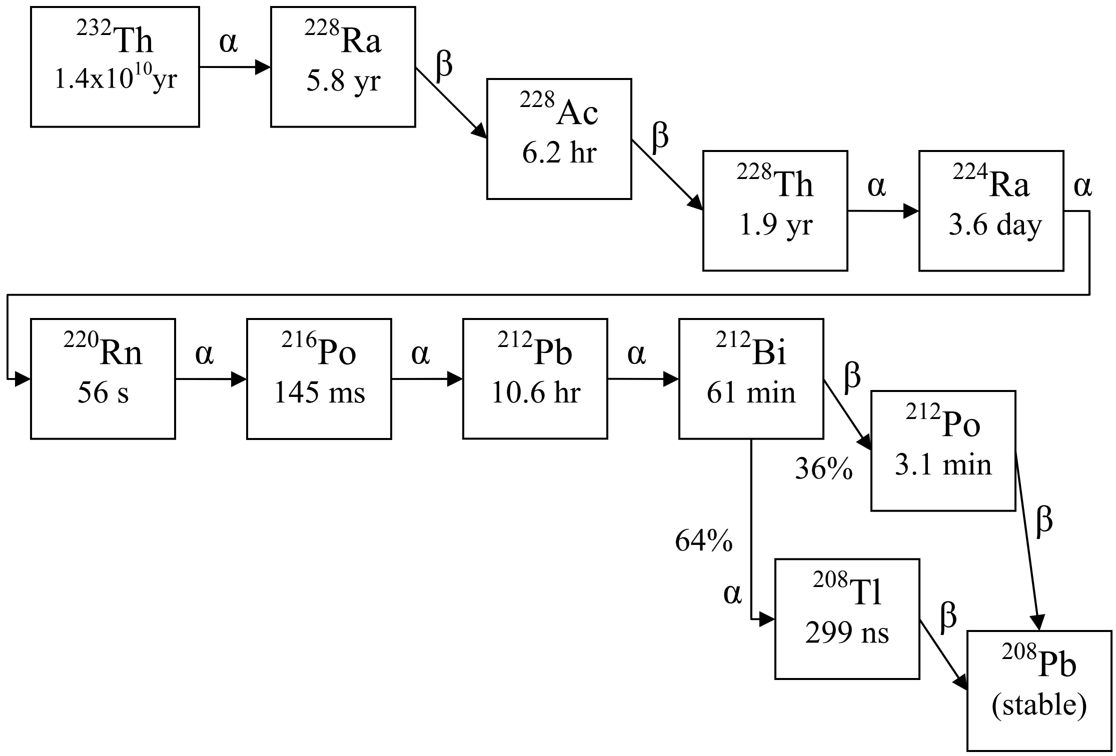

Figure 2.4: Thorium-232 decay chain

2.2.2.3 Cosmogenic Component

The interaction of cosmogenic muons in the detector materials is expected to contribute to the background rate. Muons interacting with detector materials will produce neutrons and fragments capable of producing nuclear recoil events in the argon.

The high energy muons will also produce Cherenkov radiation in the acrylic light-guides. This light will be detected by the PMTs directly. To reduce this effect, the light-guides were fabricated from acrylic doped with UV absorber.

The contribution made by these effects to the total background rate will be decreased when moving the detector underground to SNOLAB, having a rock overburden of 6.011 km (w.e.). This is expressed in units of water equivalency (w.e.), computing the density of the rock for that of water, by convention and for convenience in comparing other facilities.

A study by Hime and Mei [43] describes the reduction in the muon flux and the reduction in neutron production by cosmogenics at various underground facilities.

The total muon flux has been measured in SNOLAB, to be $(3.77 \pm 0.41) \times 10^{-10}$ cm^{-2}/s. A reduction from the surface rate, of approximately 1×10^{-2} cm^{-2}/s. As discussed in [43], the depth sensitivity relation, a ratio of the rate of neutrons produced cosmogenically, can be assigned to each underground facility, based on the observed underground neutron flux and average muon energy. Given by,

$$\begin{aligned} F &\equiv \frac{R_{\text{iso}}(\text{Surface})}{R_{\text{iso}}(\text{Underground})} = \left(\frac{4\ \text{GeV}}{\langle E_\mu \rangle} \right)^{\alpha} \frac{\phi(\text{Surface})}{\phi(\text{Underground})} \\ &= 1.67 \times 10^{6} \text{ at SNOLab} \end{aligned} \tag{2.5}$$

where the average muon energy is estimated to be 356 GeV at SNOLAB.

2.3 Background Discrimination

In order to make a sensitive dark matter search, it is necessary to have a method to reject any signal produced from spurious sources from within the signal-region of the detector. The timing characteristics of the scintillation light of de-excited argon dimers allow an excellent signal to background discrimination of electron-like particles. The demonstration of the effectiveness of this method is required in DEAP, for which its sensitivity is dependent.

2.3.1 Pulse Shape Discrimination in Liquid Argon

As described in the preceding section, a fraction of the scintillation is produced at a later time, where the fraction is dependent on the charge density of the incident particle. This leads us to a very efficient method of discriminating between different charged particles.

As discussed in section 2.1.1, excited argon dimers decay to short lived singlet states, and longer lived triplet states. Thus, the scintillation light we observe quickly reaches a peak and slowly decays away. We define the prompt light as the light within 150 ns after the event trigger, and the light there after as ‘late’ light. The prompt will be mostly scintillation produced from the de-excitation of the singlet state, though will have some component from the triplet. The late light will be mostly scintillation from the de-excitation of the triplet state.

Given the triplet to singlet ratio differs for electrons to nuclear recoils, as discussed in 2.1.2, the fraction of prompt light to the total light, here referred to as F_{Prompt}, can be used as an identifier for each event.

The discrimination must be sufficient to reject those events produced by the decay of ^{39}Ar and by decay or spallation of the detector materials. As shown in 2.2.1, the decay of ^{39}Ar will produce the most significant contribution of background events. This sets a minimum requirement of the pulse shape discrimination (PSD), summarised in Table 2.9.

Mass of Argon	Number of 20 – 40 keV events from Ar-39	PSD Required
7	3.9×10^{6}	2.6×10^{-7}
10	5.5×10^{6}	1.8×10^{-7}
100	5.5×10^{7}	1.8×10^{-8}
1000	5.5×10^{8}	1.8×10^{-9}

Table 2.9: Minimum PSD requirements due to Ar-39

In order to demonstrate the discrimination, a population of well-tagged events, of at least the number produced by background is desired. The source and tagging method for calibration are described in the next section. To make further predictions of the PSD, a thorough understanding of the detector is required, described in Chapter 4, following with predictions of the PSD in Chapter 5.

Chapter 3

DEAP Concept & Design

DEAP-1 utilises approximately 7 kilograms of liquid argon as a target for WIMP interactions. The scintillation photons produced from particle interactions within the argon are collected by photomultiplier tubes. The timing characteristics of the produced photons are used in a way to identify and discriminate each event against background, as discussed in the previous chapter. Here we describe the principle components of the DEAP-1 detector in detail. By use of a liquid target such as argon, the essential principles of this system can be scaled for a tonne-scale target mass for a WIMP sensitive search.

3.1 Hardware

The following sections will describe each component in detail. To follow the description of the detector, it will be helpful to follow or refer to the flow diagram shown in Figure 3.3.

3.1.1 Purification

We begin at the point at which argon enters the system, the first stage being the SAES purifier. The SAES unit is designed to reduce impurities within the bottled gas to lower than 1 part per billion (ppb) parts of argon [32]. The purifier works in principal by flowing gas through a heated element, which impurities chemically bind to. After passing the filter, the argon contains less than 1 ppb each for impurities of O_2, H_2O, CO, CO_2, N_2, H_2 and CH_4, by the manufacturer's standards.

Impurities would absorb photons and increase the rate of non-radiative transitions of the dimers, particularly the triplet, in effect quenching the late scintillation, as discussed in 2.1.2. The purity requirements were calculated in 2.1.3.

The argon is pressurised (at < 30 psi) throughout the system, with pressure supplied by the gas bottle, regulated by a flow controller to levels of litres per minute.

3.1.2 Cryostat

The purified argon passes the purifier, into the liquefier, which is essentially a wound ¼ inch copper tube immersed in a vessel of liquid nitrogen, 30 inches long and 8 inches in diameter, shown in Figure 3.1.

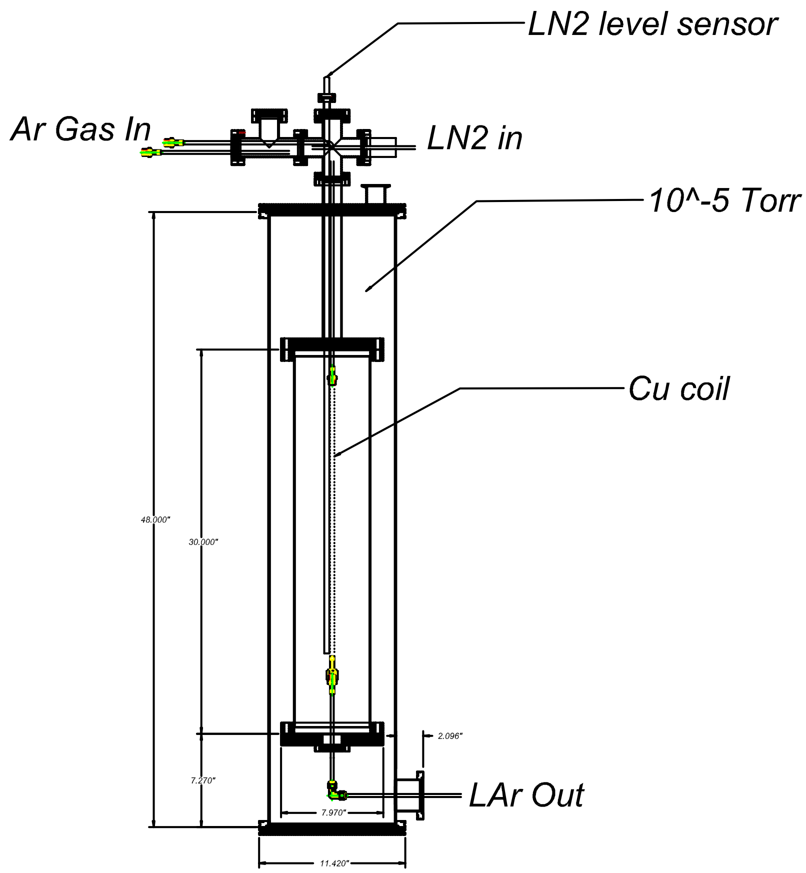

Figure 3.1: Cryostat and liquefier schematic

As the boiling point of nitrogen is 77 K and that of argon is 87 K [44], the pressure within the vessel is regulated at 34 psi to keep the argon from freezing. The saturated vapour pressure-temperature curve for nitrogen is shown in Figure 3.2, overlaid with that of argon [44] and the freezing point of argon. The triple point of argon is at a temperature of 84 K at 10 psi.

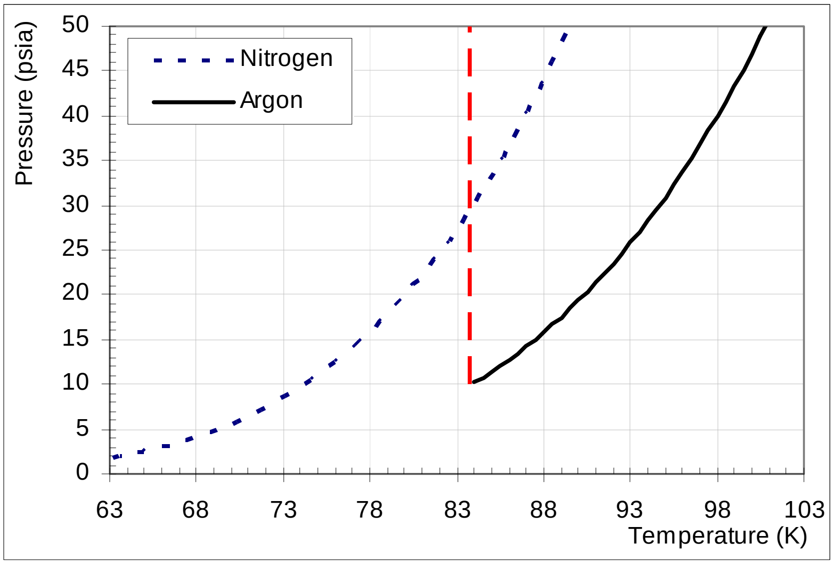

Figure 3.2 Pressure temperature curves of nitrogen and argon

The inner vessel has a connection to the inner coil, an outlet from the coil and an inlet for liquid nitrogen. By design, argon gas flows through the coil while the vessel is full of liquid nitrogen being held at a pressure of 33 psi. This liquefies the argon within the coil which proceeds to flow toward the argon chamber.

A capacitive level sensor was installed within the vessel to monitor the level of the liquid nitrogen. In order to reduce the heat load, the outside of the inner vessel is wrapped in an aluminized Mylar foil to reduce radiative heating (see section 3.1.5.1). Temperature and pressure sensors were installed to monitor the state of the nitrogen and argon.

After the coil is installed within the inner vessel, the inner vessel is housed within an outer vacuum vessel, discussed in 3.1.5, the orientation of which is indicated in Figure 3.1.

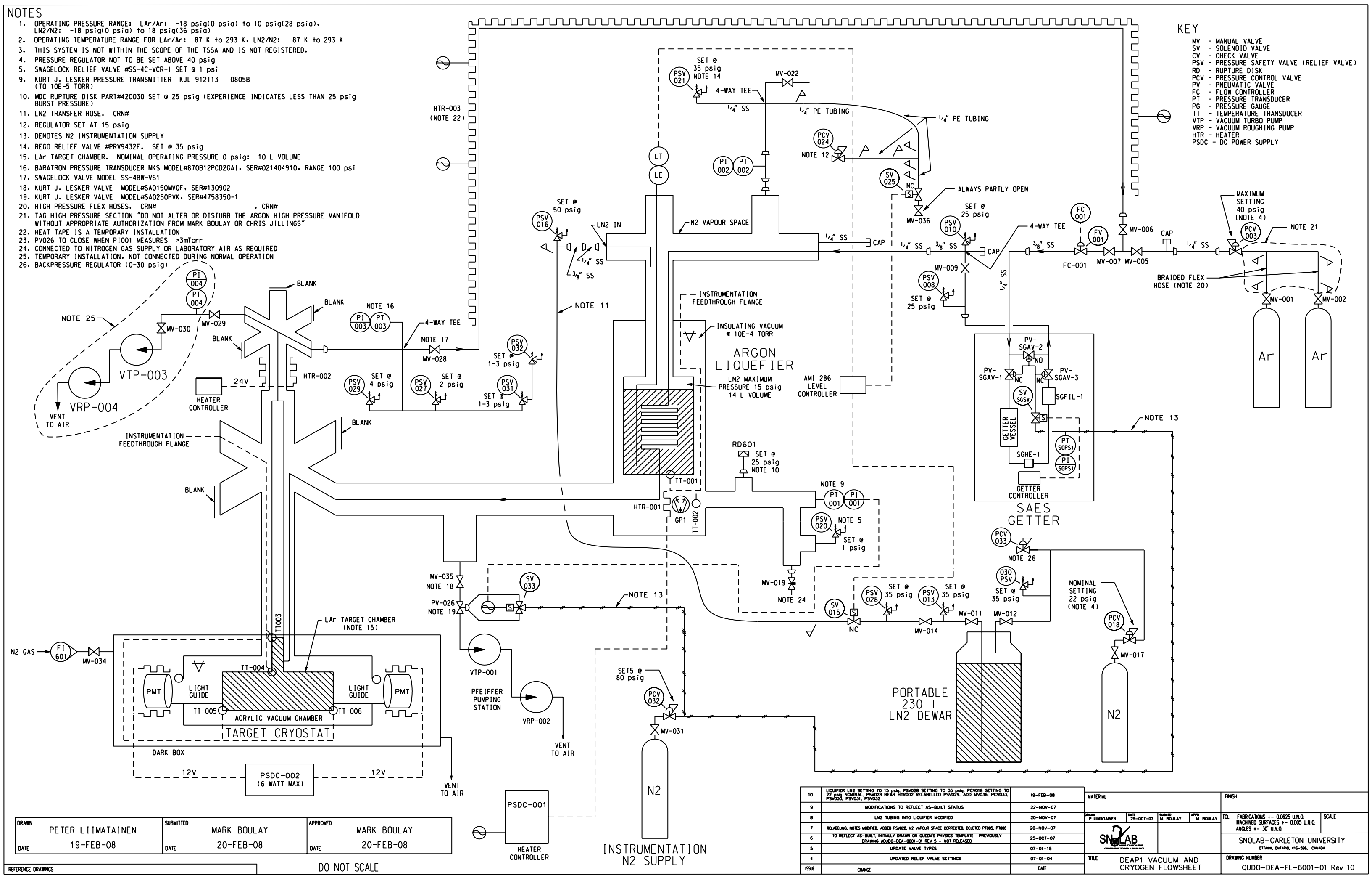

[Academic use only]

Figure 3.3: Schematic of DEAP-1 hardware

3.1.3 Argon Chamber

The target mass of argon is held in a cylindrical vessel, made of 304-stainless steel, measuring approximately 11 inches long and 5.78 inches in diameter [45], a total volume of 289 cubic inches (0.00473 m^3).

A ¼ inch thick acrylic sleeve, 11 inches long with diameter of 5.5 inches, is housed within the steel cylinder so coatings (see section 3.1.6) can be easily applied. Two glass windows [46] (glass thickness of 0.375 inches) make-up the ends of the chamber. Temperature sensors are installed on each of the glass windows to monitor the argon temperature and the stainless steel of the argon chamber is wrapped in an aluminized Mylar foil to reduce radiative heating. Figure 3.4 shows the argon chamber.

The chamber assembly holds 7.6 kg of liquid argon (given the density of liquid argon is 1430 kg/m^3 [44] and the calculated volume of the chamber assembly). Approximately 6.1 kg of the argon is in view of the photomultipliers at any time.

3.1.4 Argon Line

We refer to the argon line as the lines which feed the argon from the liquefier into the argon vessel. These pieces are seen as the horizontal and vertical components between the argon chamber and the cryostat on Figure 3.5.

Precautions regarding the purity of the argon are taken with all the piping and components the argon flows though. Stainless steel is mostly used. Where the piping attaches to other components, adaptors with metal seals are used. Lines are wrapped in super-insulation to reduce the heat load from radiative heating. Where possible, piping is heated while being evacuated to remove further impurities.

Temperature sensors are installed on the outside of the argon line at 1 inch intervals along the bottom 4 inches of the neck toward the connection to the argon chamber. These are used when filling the argon chamber for an indication of the liquid level.

The target mass of argon will boil slowly due to the residual heat load on the system. A line was installed to recirculate this argon into the liquefier so that the system is closed and no argon is lost while running, see Figure 3.3.

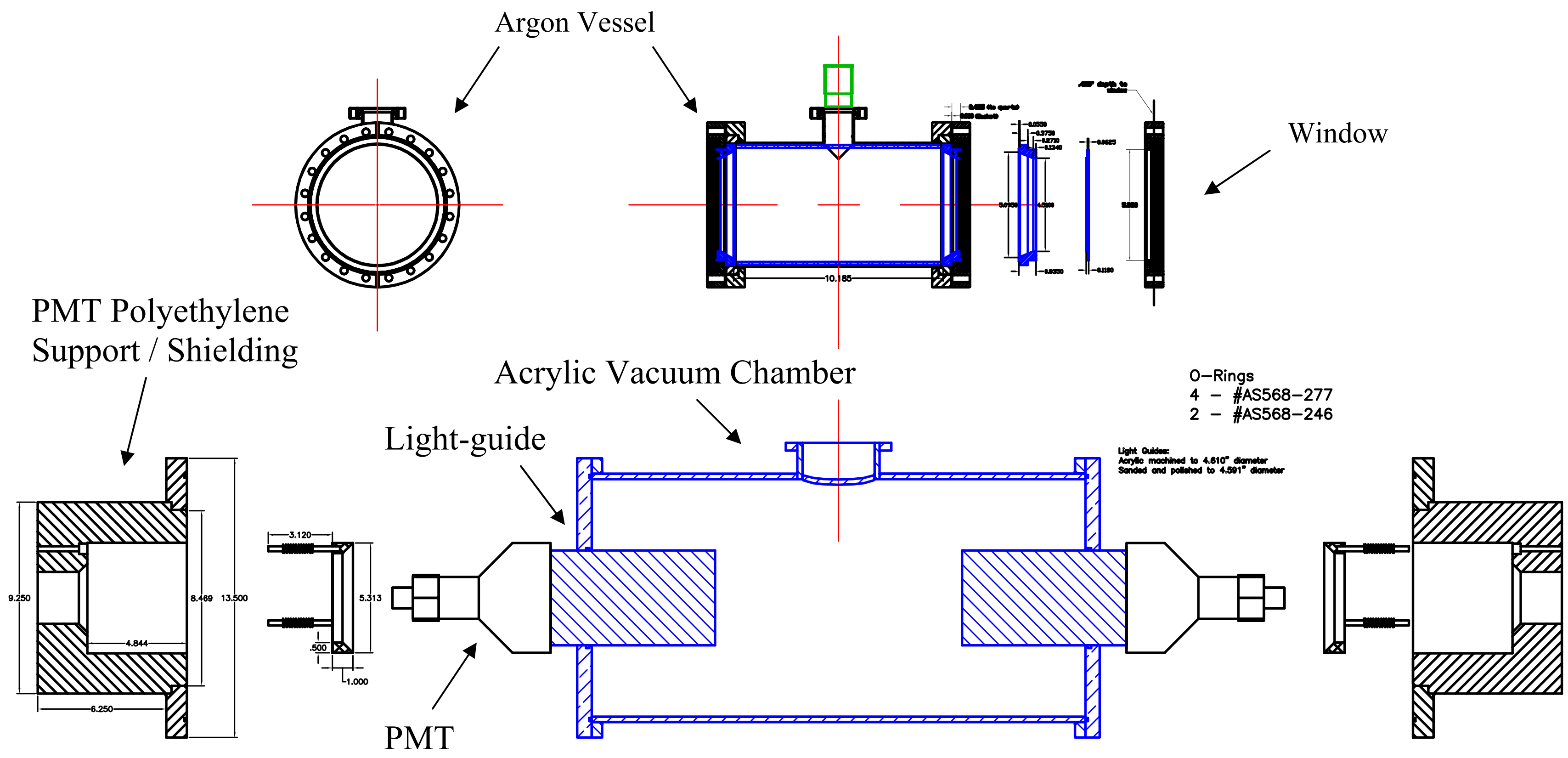

Figure 3.4: Full argon chamber assembly

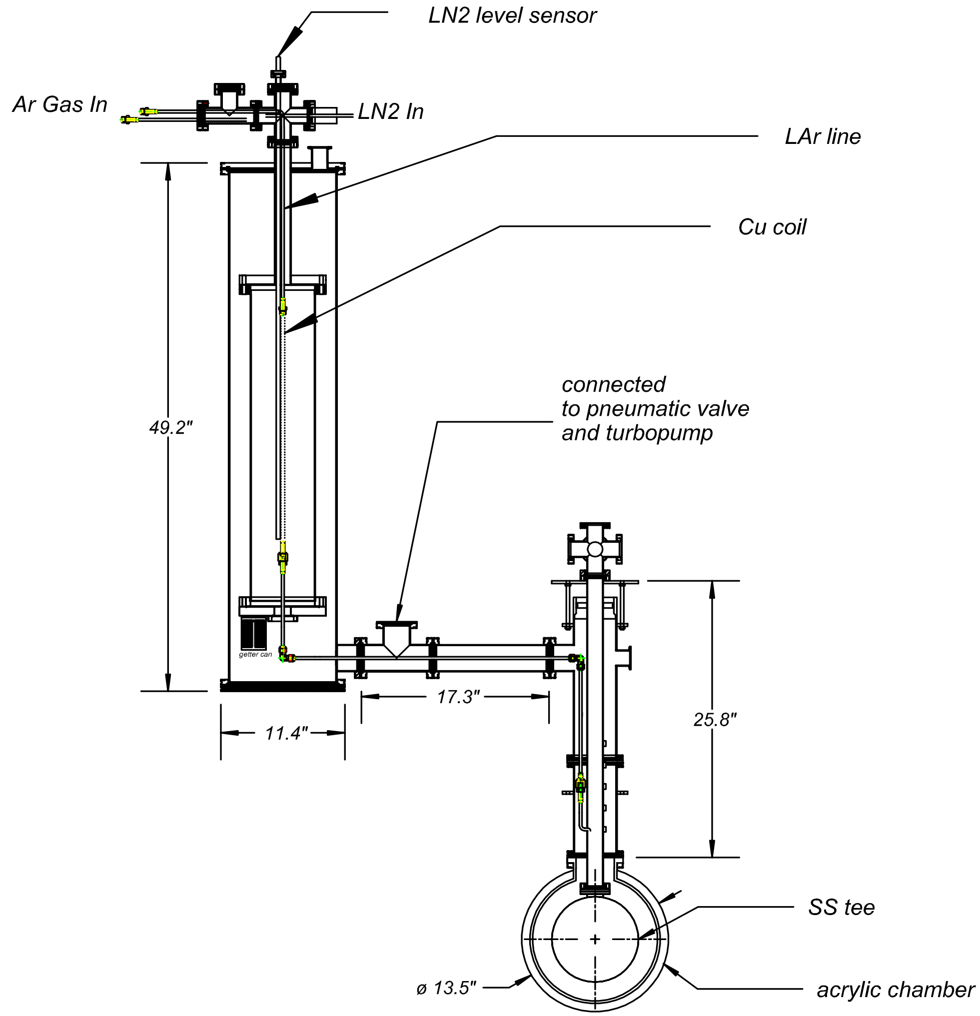

Figure 3.5 Cryostat and detector assembly

3.1.5 Insulating Vacuum

To thermally insulate the argon chamber and liquefier, both of which operate at cryogenic temperatures, the components were completely housed within a larger evacuated container.

The insulating vacuum is built around the detector components using mostly larger piping (KF and ISO fittings). The liquefier and inner liquid nitrogen vessel are contained in a larger steel cylinder, of length 40.2 inches and 11.4 inches in diameter. The liquefier is supported from the top face of this outer vessel. Refer to Figure 3.1 and Figure 3.5 for their orientation.

To house the argon chamber, a larger chamber of acrylic was built, 25.4 inches long and 13.5 inches in diameter. Acrylic was chosen for this component for having fewer radioactive impurities. The acrylic chamber is shown in relation to the argon chamber in Figure 3.4.

We now estimate the residual heat load on the components inside the vacuum in a similar manner as was done for DEAP-0 [47].

3.1.5.1 Radiative Heating

Radiative heating is one process by which heating of the inner components will occur. The transfer of thermal radiation from the surface of the vacuum insulation to those surfaces being held at 85 K will be significant as the transfer is a function of the difference of the inner and outer surface temperatures to the fourth power, given by,

$$\dot{Q}_r = F_e F_{1-2} \sigma A_1 \left(T_2^4 - T_1^4 \right) \tag{3.1}$$

where 1 represents the inner surface and 2 the outer surface, and,

- F_e is an emissivity factor,
- F_{1-2} is a geometrical factor, though here equal to one with the inner vessel being completely contained within the outer vacuum,
- σ is Stefan-Boltzmann's constant (56.69 nW/m^2/K^4)
- A is the surface area (m^2)
- T is the temperature (K)

The emissivity factor is given by,

$$\frac{1}{F_e} = \frac{1}{\varepsilon_1} + \frac{A_1}{A_2}\left(\frac{1}{\varepsilon_2} - 1\right)$$

where ε is the emissivity of the material. The properties used in these calculations are summarised in Table 3.4.

The emissivity of stainless steel is 3 times higher than that of aluminium at 80 K. To help reduce radiative transfer each inner surface was wrapped in more than one layer of an aluminized Mylar foil.

The radiative heat for each of the inner components is listed in Table 3.1, with the calculations for the case where the inner surfaces have the properties of aluminium, and again for bare stainless steel. The true value should be within these values as the wrapping of some components was not ideal due to the difficulty in covering their geometry.

Component		Heat Load (W)
Liquefier	Bare Stainless	14.3
	Aluminized foil	4.8
Argon Line + neck	Bare Stainless	2.5
	Aluminized foil	0.8
Argon chamber	Bare Stainless	4.5
	Aluminized foil	1.4
Total	Bare Stainless	21.3
	Aluminized foil	7.1

Table 3.1: Radiative heat load to inner components

3.1.5.2 Conductive Heating through Material

The conduction of heat from the outside surfaces to the inner can occur through the components supporting the inner components. The liquefier is supported from the top of the outer vacuum vessel by tubing of 1.5 inches in diameter, 18 inches long. The argon chamber is supported by the argon neck, 1.5 inches in diameter, 29 inches long, seen in Figure 3.5.

The light-guides, 5.8 inches (14.8 cm) in diameter and 8.2 inches (20.8 cm) long, feed through the acrylic chamber and press up against the glass windows of the argon chamber. The mean thermal conductivity of acrylic is relatively low, at 0.2 W/m/K compared to stainless steel at 12.67 W/m/K however the light-guides are responsible for the largest single heat load to the chamber. The conduction through the PMT and other signal cable feed-throughs is assumed to be negligible.

The heat goes as a function of temperature given by,

$$\dot{Q}_c = \frac{kA(T_h - T_c)}{L} \tag{3.2}$$

where T_h represents the temperature of the hot surface, T_c the cold (inner) surface, and k is the mean thermal conductivity.

The heat load by conduction through a light guide is,

$$\begin{aligned}\dot{Q}_c &= \left(0.2\frac{\mathrm{W}}{\mathrm{m}\cdot\mathrm{K}}\right)\left(\frac{\pi\cdot 0.148\ \mathrm{m}}{2}\right)^2 (300\ \mathrm{K} - 87\ \mathrm{K}) \Big/ (0.208\ \mathrm{m}) \\ &= 3.5\ \mathrm{W}\ \text{(per lightguide)}\end{aligned} \tag{3.1}$$

Results for all components in contact with the outer vacuum are summarised in Table 3.2.

Component	Heat Load (W)
Liquefier	4.84
Argon chamber	11.31
Total	16.15

Table 3.2: Heat conduction through component supports

3.1.5.3 Heat Transfer by Gas Conduction

The residual pressure within the evacuated region will conduct heat from the outer surfaces to the inner cold surfaces. A Pfeiffer turbo-molecular pump, with a rated pumping speed of 60 lpm_{N2} and an ultimate pressure of less than 1×10^{-7} mbar (8×10^{-8} Torr) [47], was used to hold the outer vacuum. Here we calculate the heat load on the system due to the conduction of heat by the molecular flow of gas as a function of the residual pressure. This is given by,

$$\dot{Q}_{gc} = GA_1 p\left(T_2 - T_1\right) \tag{3.2}$$

where,

- p is the residual gas pressure in the evacuated region,
- G is given by [47],

$$G = \frac{\gamma+1}{\gamma-1}\left(\frac{gcR}{8\pi T_1}\right)^{1/2} F_a$$

- γ is the specific heat ratio for the contained gas (for air, 1.4),
- R is the specific gas constant (for air, 286.9 J/kg K)
- F_a is an accommodation factor given by [47],

$$\frac{1}{F_a} = \frac{1}{a_1} + \frac{A_1}{A_2}\left(\frac{1}{a_2} - 1\right)$$

The sum of this heat load to the liquefier, argon line, inner neck and the argon chamber is shown as a function of pressure in Figure 3.6.

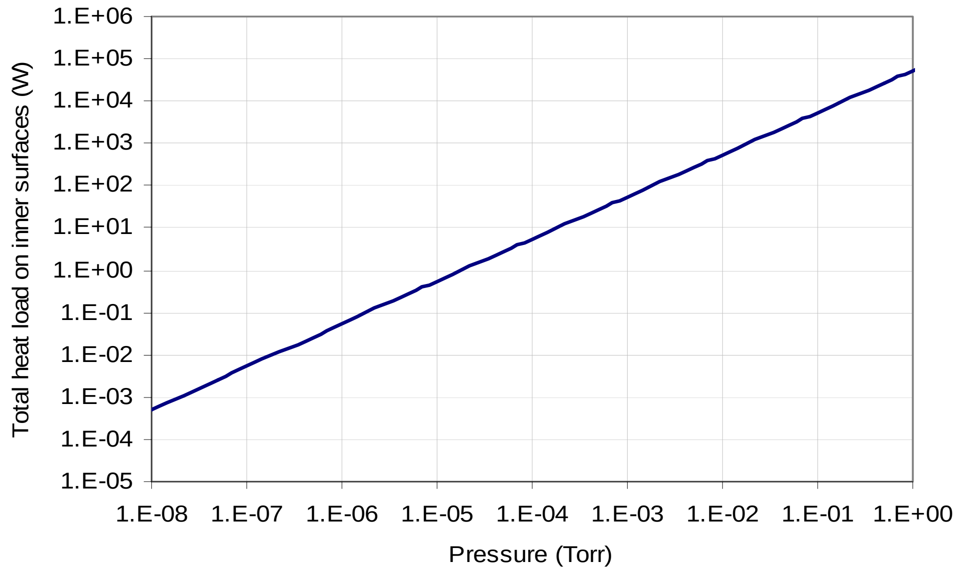

Figure 3.6: Heat transfer of inner components by gas conduction

While in operation the outer vacuum was held stable at 0.1 mTorr, leading to a heat load on the total system of 5.3 W.

3.1.5.4 Sum of Heating Processes

The sum of these three processes gives an estimate of the total heat load on the inner components of 29 W, summarised in Table 3.3.

Component	Heat Load (W)		
	Radiative*	Solid conductive	Gas conductive
Liquefier	4.8	4.8	3.6
Argon line + neck	0.8	(neg)	0.6
Argon Chamber	1.4	11.3	1.1
Total	7.1	16.2	5.3
Overall Total	28.6		

Table 3.3: Total heat load on inner components, summary

***assuming the inner surfaces wrapped in aluminium**

Given the latent heat of vaporization for liquid argon is 161.9 kJ/kg and that for nitrogen is 199.3 kJ/kg we can estimate the rate at which each liquid will boil-off,

$$R_{\text{boil}} = \text{applied heat load} \,/\, \text{latent heat} \tag{3.3}$$

$$\begin{aligned} R_{\text{boil,N2}} &= 14.0\ \text{W}/199.3\ \text{kJ/kg} \\ &= 6.05\ \text{kg/day} \\ &= 3.4\ \text{slpm} \end{aligned} \qquad \begin{aligned} R_{\text{boil,Ar}} &= 14.5\ \text{W}/161.9\ \text{kJ/kg} \\ &= 7.8\ \text{kg/day} \\ &= 4.3\ \text{slpm} \end{aligned}$$

The argon is enclosed within a closed system where the argon boil-off is returned to the liquefier. The circulation through the return line, measured with a calibrated flow meter, was found to vary within 3 - 5 slpm, in agreement with the estimation.

The volume of the liquefier is sufficient to hold approximately 20 L of liquid nitrogen and was refilled when 1/3rd of this had been used to ensure some portion of the liquefier's coil was always submersed. While in operation this vessel was typically refilled every 7 - 8 hours, which approximates to a boil off rate of 13 slpm (23 kg/day). The discrepancy in the nitrogen boil off rate, equivalent to 38 W, is due to the liquefaction of the re-circulated argon and inefficiencies.

The properties used in the calculations in this section are listed in Table 3.4 and Table 3.5.

Property	Symbol	Value
Cold side Temperature	T_c, T_1	87 K
Hot side Temperature	T_h, T_2	300 K
Mean thermal conductivity of 304 SS	k	12.67 W/m/K
Thermal conductivity of acrylic	k	0.2 W/m^2 K
Emissivity of Al (80K)	ε_1	0.0183
Emissivity of Al (300K)	ε_2	0.03
Emissivity of 304 SS (80K)	ε_1	0.06
Emissivity of 304 SS (300K)	ε_2	0.15
Component Surface Areas:		
Liquefier surface area	A_1	0.609 m^2
Outer vacuum surface area	A_2	1.27 m^2
Argon line + Neck inner lines	A_1	0.099 m^2
Argon line + Neck outer vessel	A_2	0.393 m^2
Chamber surface area	A_1	0.175 m^2
Acrylic Chamber surface area	A_2	0.880 m^2
Dark box surface area	A_2	5.20 m^2

Table 3.4: Material thermodynamic properties [47]

Property	Symbol	Value
Ratio of specific heats	γ	1.4
Geometric factor	g_c	1.0
Specific Gas Constant	R	287
Accommodation coefficient at 80 K	a_1	1.0
Accommodation coefficient at 300 K	a_2	0.85

Table 3.5: Thermal properties of air [47]

3.1.6 Wavelength Shifter

Scintillation light from argon is produced in the high UV at 128 nm (see chapter 2). The efficiency of the photomultipliers and transmittance of glass is low at these wavelengths. The wavelength shifting compound, tetraphenyl butadiene (TPB) [49] was used to shift the 128 nm photons to 440 nm [50], the wavelength at which the PMTs run optimally. The coating for the argon chamber is applied to a thin acrylic sleeve, while the coating on the windows is applied directly to the glass.

To collect the light efficiently, the inner acrylic sleeve of the argon chamber is coated first with a reflective paint (95% reflective at 440 nm [51]) made of TiO_2, shown in Figure 3.7. The thin film of TPB was then applied to the windows and acrylic components by vacuum deposition.

The deposition was achieved by heating a mass of TPB which was then left to solidify onto a small coil of wire. The mass of TPB on the coil, windows and acrylic components were weighed to within 1 milli-gram. Each component was placed into a vacuum chamber along with the TPB coil, at a sufficient distance to ensure a uniform coating. When the pressure within the chamber had been reduced to less than 1 mTorr, a current (of approximately 4 amps) was passed through the coil, slowly evaporating the TPB. The components were weighed after to determine the amount of mass of TPB per unit area. For the windows, 8 ± 2.8 mg was evaporated over 3 hours (and 9 minutes) for a coating of 0.063 ± 0.022 mg/cm^2. It was intended to evaporate a thickness of 0.3 mg/cm^2 onto the acrylic sleeve, however measuring the weight of the TPB applied to the acrylic sleeve proved difficult due to a significant mass of absorbed water in the acrylic evaporating when being placed in the vacuum chamber, hence the chamber weighed less after evaporation and the coating thickness largely uncertain. The coating was applied over 3 hours and a similar faint film was observed.

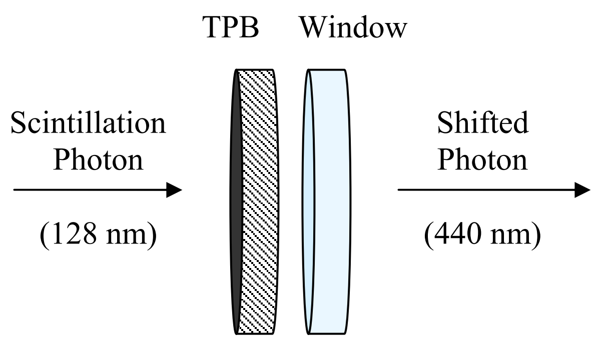

Figure 3.7 Chamber, window coatings

3.1.7 Light-guides

There are practical constraints, as well as design specifications which a light guide provides a nice solution to. It is desired to remove the PMTs from contact with liquid argon temperature, as running the PMTs cold is difficult experimentally and their performance at cryogenic temperature is reduced [52]. The PMTs are also a source of background radiation and hence would be better located at a distance from the argon.

Cylindrical light-guides, 5.8 inches (14.8 cm) in diameter and 8.2 inches (20.8 cm) long, of cast acrylic were fabricated. Acrylic propagates light efficiently and has an index of refraction of 1.46 [40], which is closely matched to glass, helping to reduce reflections at the interface with the glass window. Acrylic was selected for being low in radioactive impurities [40] in order to help reduce background events.

Acrylic doped with UV absorber (UVA) was selected, to help reduce the background from Cherenkov radiation produced by through-going muons cosmic (section 2.2.2.3).

An initial investigation to measure the bulk attenuation measured a coefficient of 0.14 cm^{-1} at 440 nm. This gives a transmittance of roughly 70% for an 8 inch light guide. The attenuation is higher than plain acrylic due to the absorber. When moving the detector underground to SNOLAB, the cosmic background is reduced, hence new light-guides of plain cast acrylic were fabricated.

Acrylic conducts heat poorly, with a thermal conductivity of 0.2 W/m^2 K, allowing the light-guides to be installed in contact with the glass windows at 87 K at one end, and the PMTs at room temperature at the other, with little heat conduction (see section 3.1.5.2). This assembly is shown in Figure 3.4 and Figure 3.8.

Hence an 8 inch long light guide allows the PMTs to be at a sufficient distance from the chamber to minimise background radiation, minimises the heat load to the chamber and allows their operation at room temperature.

3.1.8 Photomultiplier Tubes

Two Electron Tubes 9390 photomultipliers (PMTs) [53], each with diameter of 5 inches, were installed. The manufacturer's specifications state these tubes have 25% quantum efficiency at 440 nm. The tubes were run typically at 1550 V.

The PMTs were housed in a carved block of polyethylene for shielding and to hold the PMTs onto light-guides. Figure 3.8 shows this assembly.

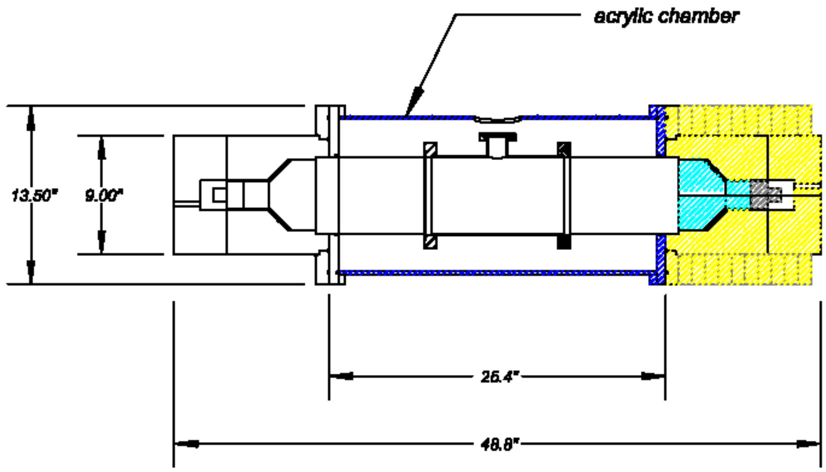

Figure 3.8 Chamber final assembly

3.1.9 Calibrated Source – Annulus

In order to demonstrate the required pulse shape discrimination, a sufficient population of events was required. To efficiently collect such a population, we require a calibrated source and a trigger system to track the time of each decay.

A segmented detector, here named the annulus, consisting of 4 NaI detectors configured together, was used to setup a multi-coincident tag with a Sodium-22 source. Another separate PMT with a 2 inch NaI crystal was placed in the centre of the detector, at the back behind the source. Lead shielding covers all sides but the front face. See Figure 3.9 for a schematic.

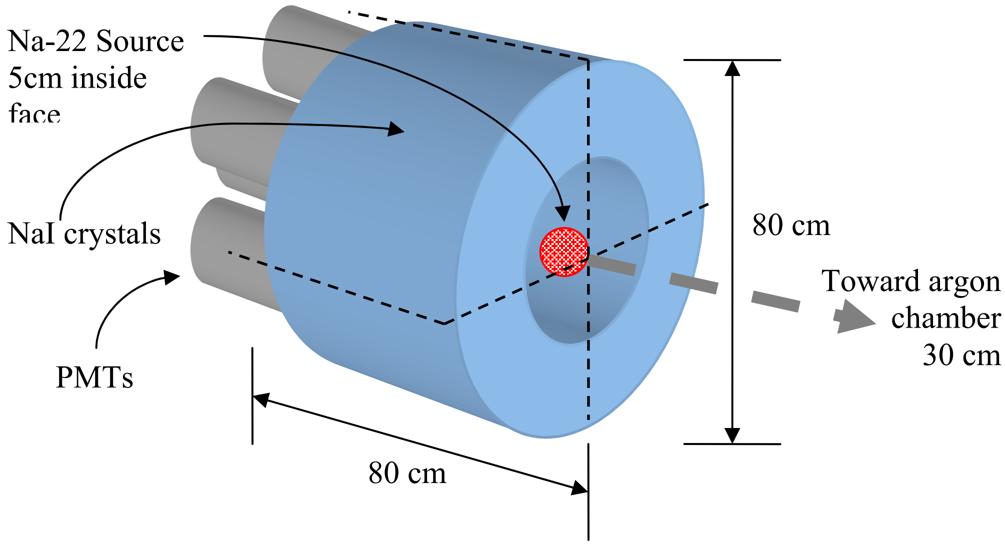

Figure 3.9: Annulus assembly (not to scale)

The source is placed along the centre line of the annulus, while the annulus is situated side-on to the argon chamber.

Sodium-22 decays by emission of a beta-plus particle, shown in Figure 3.10.

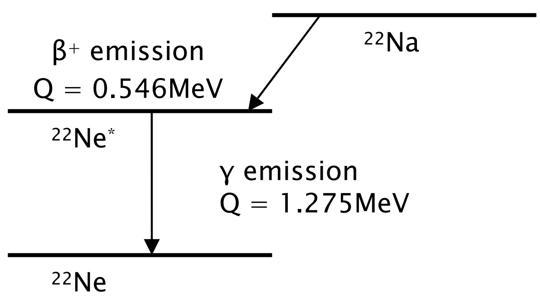

Figure 3.10: Na-22 decay scheme

By conservation of momentum, we expect two gammas travelling in opposite directions produced from the annihilation of the beta-plus particle. The 1.275 MeV gamma from the de-excitation of the daughter is emitted isotropically; hence the source is placed within the annulus. A tagged event is triggered when the energy of one of the annihilation gammas is detected by the centre PMT of the annulus, and the 1.275 MeV gamma is detected by one of the other crystals. The remaining annihilation gamma travels forward , toward the argon chamber. A single Na-22 decay is recorded when the annulus tag of the 1.275 MeV gamma and the backward annihilation gamma, is in coincidence with the scintillation event detected by both DEAP PMTs. The multiple coincidence for each decay provides a very well-tagged source of events [54].

3.1.10 Shielding

In order to shield the detector from local sources of background, such as those created cosmogenically in construction materials and surrounding materials, the target mass of argon was surrounded by water shielding.

Nuclear recoil events of 20 – 40 keV are of interest, given by equation (1.3), for a WIMP search. Shielding is required to stop of particles which would deposit this energy from entering the argon. Gamma events have a low fraction of prompt to late light. Neutrons of sufficient energy to produce an argon nuclear recoil are of main concern as they have a large enough mean free path to penetrate into the detector from an outside source. Taking the reported [24] quenching factor into account this suggests neutrons of approximately 0.5 – 5 MeV are problematic. In this energy range, neutrons travel their Fermi age, of 26 cm [55] on average, before being thermalised. Though, this number can vary due to the neutron cross-section in water being heavily dependent on energy and the ability of neutrons being able to capture on water.

To ease construction, the shield was built from approximately 336, 20 litre (1 cubic foot) water containers, stacked to surround the detector two layers thick to provide water shielding two feet thick. Each container had a plastic 20 litre bladder tightly packed inside a 1 cubic foot cardboard box and were filled with purified water.

Recycled plastic boards were used to fill small areas and gaps in the water layer, compressed in the form of 2 × 4 inch boards, 1 inch thick, also capable of shielding neutrons being another highly hydrogenous material.

3.1.11 Infrastructure

The argon chamber assembled with PMTs and the PMT polyethylene shields, measures 49 inches long and 13.5 inches in diameter, as shown in Figure 3.8. This whole assembly is housed within an aluminium light-tight box measuring 6 feet long × 2 feet high × 2 feet wide. The water shield was constructed around the dimensions of the dark box. The water shielding increases the minimum footprint to approximately 10 feet × 6 feet × 6 feet. The volume of water weighs a total of 9.4 tons. Substantial infrastructure is required to support this weight. The mass of the detector components are significantly less. A steel frame was used to support the mass of the water shield, while an aluminium frame was constructed to independently support the detector and its components. With the infrastructure, the overall footprint increased to 10 feet × 8 feet × 8 feet.

In constructing the detector, the aluminium and steel framing are in place first in order to rig the detector components from them.

3.2 Electronics

All signal processing was achieved using nuclear instrument modules (NIM). The schematic for the trigger electronics is shown in Figure 3.11 and can be categorised into three main sections: the coincidence of the detector PMTs, the high energy cut and the coincidence with the annulus.

A GHz LeCroy oscilloscope [56] was used to record the voltage trace for each PMT of each event over 10 μs at 1 ns resolution. The use of a RAM disk as intermediate storage between the oscilloscope and hard disk helped to increase the rate at which data could be recorded.

The coincidence of the detector PMTs was fed into the trigger system, as shown in Figure 3.11. To reduce pileup of events, a coincidence was delayed by 10 μs before the next coincidence.

A high energy cut was used to remove events of higher energy than of interest and as a muon-veto. The summed PMT signal was fed into a single channel analyser (SCA) which was tuned to cut events of greater than 300 photoelectrons. For energy calibration, the SCA cut was not used so that the full energy spectrum could be recorded.

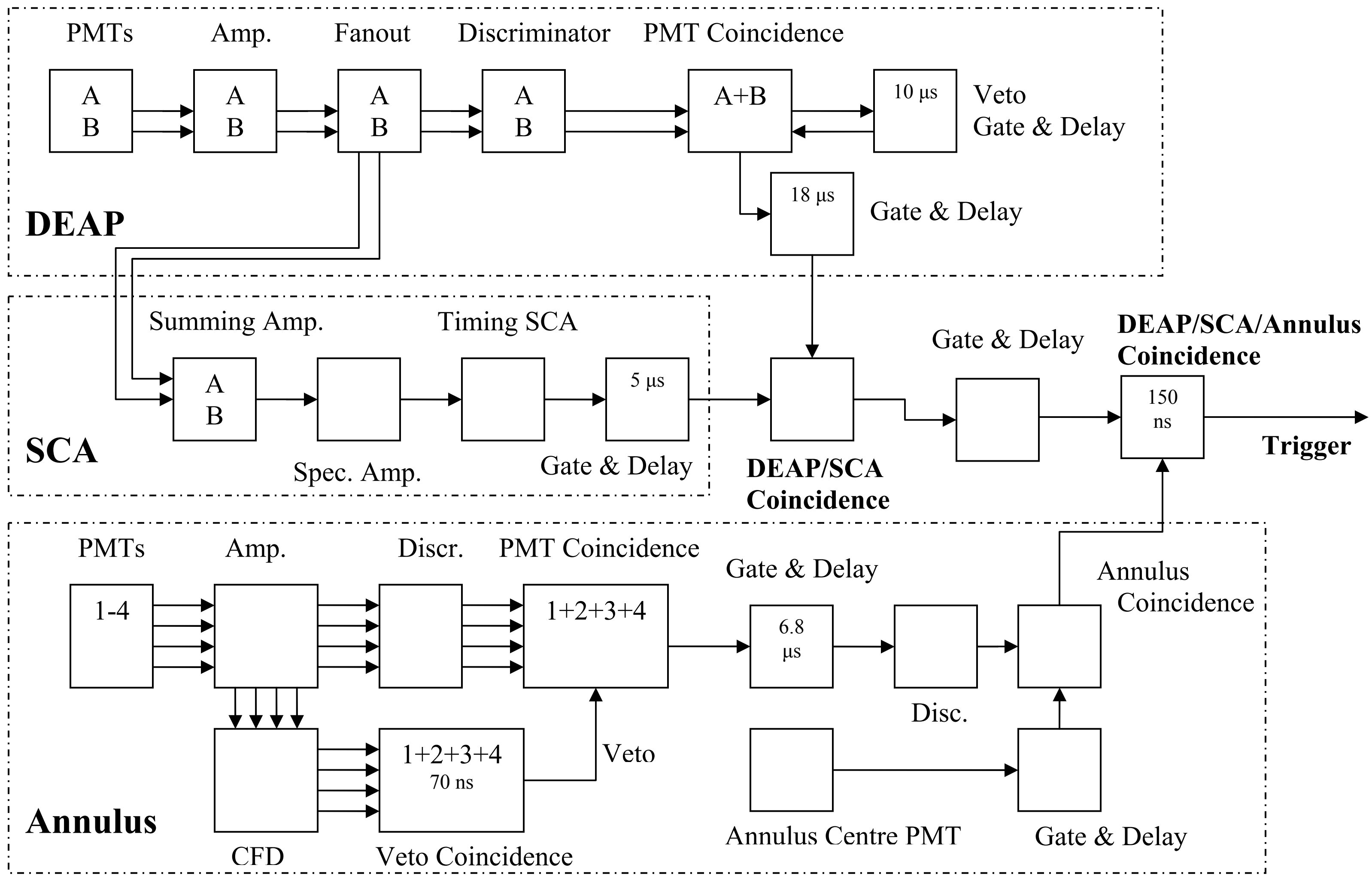

Figure 3.11: Electronics schematic [54]

The four segment PMTs of the annulus, as described in section 3.1.9, were tuned to detect the energy of the 1.275 MeV gamma, while the centre PMT detects the 511 keV annihilation gamma. For Na-22 calibration, the coincidence of the annulus PMTs and the detector PMTs (after the SCA cut) is used as the trigger for events. For background and Am-Be calibration, only the coincidence of the detector PMTs was used for the trigger.

3.3 Operation

3.3.1 Argon Chamber

The temperature of the argon, measured by sensors on the glass windows, was observed to be very stable, within 2 - 3 degrees, with variation only due to the temperature and pressure changes during the filling cycle of the liquid nitrogen in the cryostat.

The residual heat load on the argon caused argon to boil-off producing a circulation of gas through the return line at approximately 5 litres per minute.

3.3.2 Cryostat

The pressure of the nitrogen vapour inside the liquefier was regulated at 33 psi, to keep the temperature above the freezing point of argon, as stated in 3.1.2. A variation of typically no more than 2 degrees was observed in measurements of the temperature of the inner vessel and the liquid nitrogen. An automatic controller with feedback from the liquid nitrogen level sensor was used to fill the inner vessel when low.

3.3.3 Vacuum Insulation

The vacuum insulation was stable, with small variation only due to the temperature and pressure changes during the filling cycle of the liquid nitrogen in the cryostat.

3.3.4 Phototubes

The gain of the phototubes was optimised while running the tubes at 1550 V. The temperatures of the PMTs were observed to decrease slowly, due to the conduction of heat through the light-guides in contact with the argon chamber. A small heating wire was applied to the phototubes, to supply a few Watts of heat, to compensate the cooling of the tubes and the cooling of the end of the light-guides. The coefficient of expansion of acrylic is relatively large, quoted within $(55 - 76) \times 10^{-6}$ [57]. Heating was provided to ensure the integrity of the o-ring seal of the outer vacuum around the acrylic light-guides was not compromised in the event the acrylic cooled and reduced in size.

Chapter 4

Detector Performance & Analysis

The discrimination of events in experiments seeking to detect dark matter must effectively remove all background events as the expected number of WIMP events is low. The pulse shape discrimination is demonstrated using a population of well-tagged gamma events provided by the annulus. Particles incident within the argon are identified by their characteristic light properties as discussed in Chapter 2.

Here we discuss the detector performance and response. We begin by describing the method used to identify events and the process of data cleaning, followed by the energy calibration and stability and the observed spectrum of background events.

4.1 Event Identification

4.1.1 Defining the Fraction of Prompt Light

To begin examining the light output in order to identify events, we define a parameter, here named the 'prompt fraction' (F_{Prompt}) simply as the number of promptly emitted photoelectrons to the total number of photoelectrons per event, i.e.

$$F_{Prompt} = \frac{\text{prompt photoelectrons}}{\text{total photoelectrons}} \tag{4.1}$$

In order to define this ratio we must set time intervals over which to count the photoelectrons. In computing the number of photoelectrons within the prompt peak, the voltage waveform was integrated from 50 ns before the event trigger time and 100 ns after the trigger. The late component is the integral from 100 ns after the trigger to 9 μs after the trigger. The number of photoelectrons within the integral is computed using a single photoelectron calibration, which will be discussed in section 4.2.2.

4.1.2 Gamma Events

For an incident gamma ray, the scintillation light contains a larger fraction of light that is produced later in time due to triplet states being populated which have a longer lifetime (see section 2.1.2). Figure 4.1 displays the digitised raw spectrum of a likely gamma candidate with an F_{Prompt} ratio of 0.3.

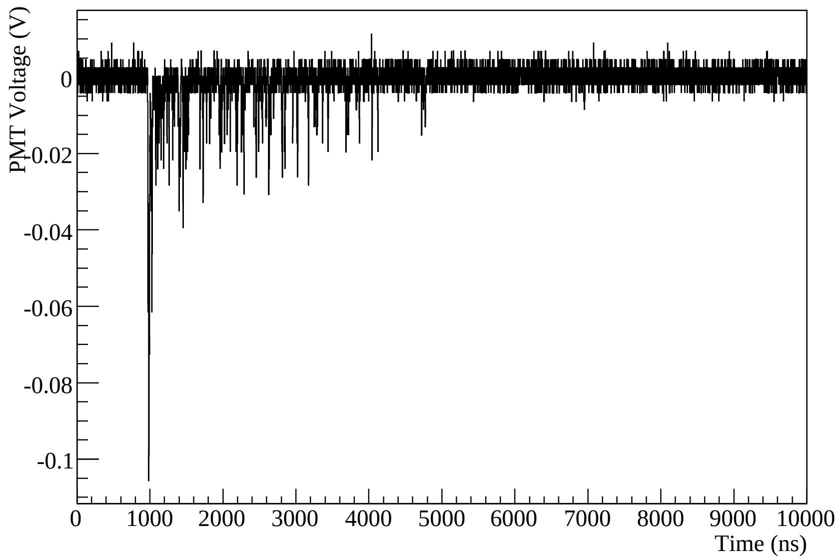

Figure 4.1 A gamma event

Note the large number of photoelectron peaks present many microseconds after the initial peak.

The gamma event shown in Figure 4.1 was produced by the Na-22 source for gamma calibration. As discussed in section 3.1.9, the source was positioned in the annulus and the annulus wheeled within inches of the side of the dark box so that the source was in-line with the centre of the detector. The decay scheme of Na-22 was presented previously in Figure 3.10.

4.1.3 Neutron Events

The detector response to a nuclear recoil event was calibrated using an ^{241}Am-^{9}Be neutron source. In an Am-Be source, alphas from the decay of americium-241 produce neutrons on a beryllium nucleus, known as (α, n) reactions. A relatively flat spectrum of neutrons up to 11.4 MeV is obtained [58], along with several gammas [59]. The decay scheme is shown in Figure 4.2.

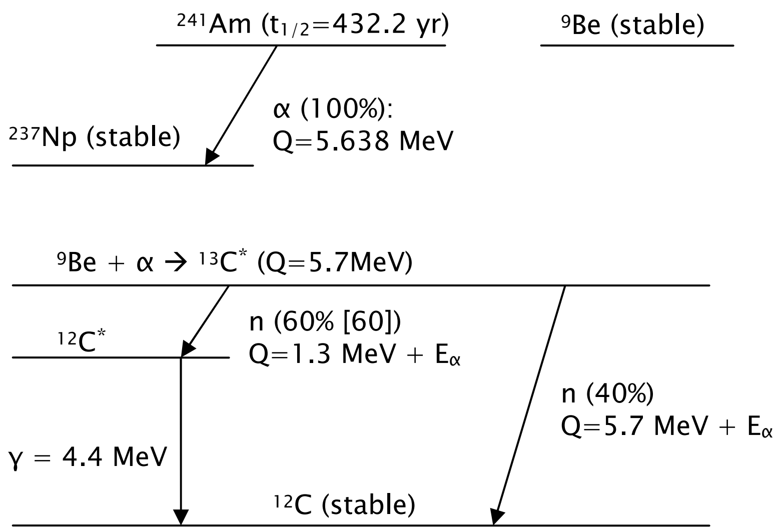

Figure 4.2 The decay scheme of an ^{241}Am-^{9}Be source

The scintillation light is mostly produced within the prompt interval, leading to higher values of F_{Prompt}. Figure 4.3 displays the digitised raw spectrum of a likely neutron candidate with an F_{Prompt} ratio of 0.8, produced by the Am-Be source for neutron calibration.

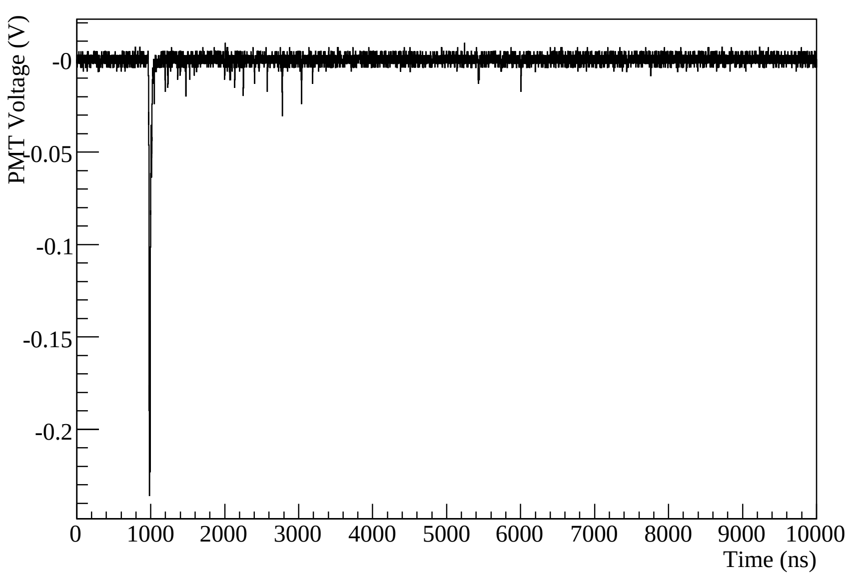

Figure 4.3 A neutron-like event.

4.1.4 Event Populations used in Analysis

After refining and testing of the detector and hardware had been completed, the detector ran fully operational from the 20th of August until the 16th of October 2007 on surface before being disassembled and shipped underground to its current location in SNOLAB. Routine gamma and neutron calibration data were taken with the Na-22 and Am-Be sources. Here we discuss the final gamma and neutron populations collected.

To demonstrate the pulse shape discrimination up to the limit achievable on surface (see section 5.1), a population of 10^9 gamma events was desired. Events in the energy range of interest are those having a scintillation yield of more than 120 photoelectrons and less than 240 photoelectrons. This range of photoelectrons would have covered the energy region of interest (20 – 40 keV) for a WIMP sensitive search, had the light yield been larger, of up to 6 photoelectrons/keV, as was expected. However a yield of only 2.8 photoelectrons/keV was measured corresponding to an energy range of 43 - 86 keV. A similar, yet lower light yield was measured in the WARP 2.3 litre liquid argon detector [24] of 2.35 photoelectrons/keV.

The rate of events in the annulus was on the order of 1 kHz. After the multi-coincidence events were recorded at a rate of 50 Hz. Subsequently, over a period of 20 days (16.2 days livetime), a total of 31.4 million gamma events (after data cuts) were collected in an almost 3 consecutive week period [61], of which, 15.8 million events fell within the energy region of interest. The population is shown in Figure 4.4 before and after data cleaning cuts were applied to the data.

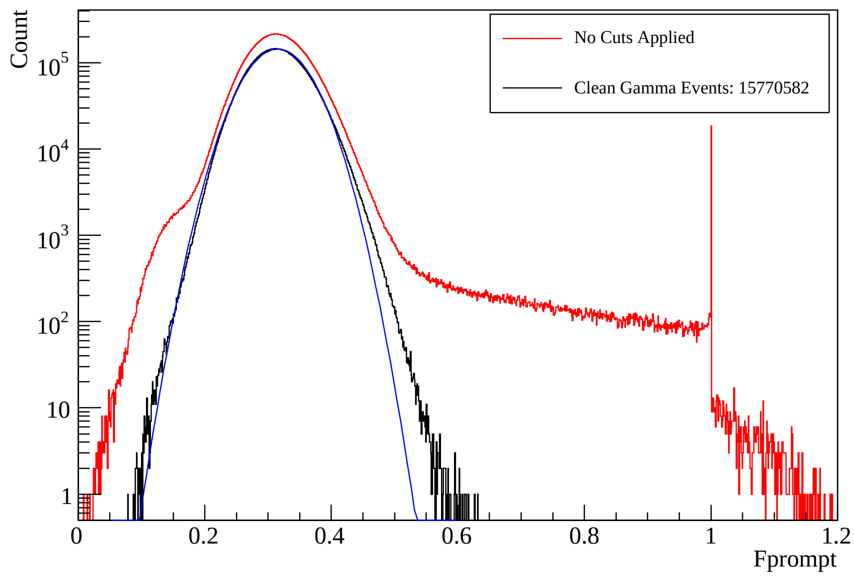

Figure 4.4: Population of ^{22}Na gamma population

A Gaussian was fit to the data, shown in Figure 4.4. Note the deviation from the Gaussian in the extra width of the tail in the data. This distribution is better described by a function discussed in section 5.1.

The total event population up to 500 photoelectrons is shown in Figure 4.5

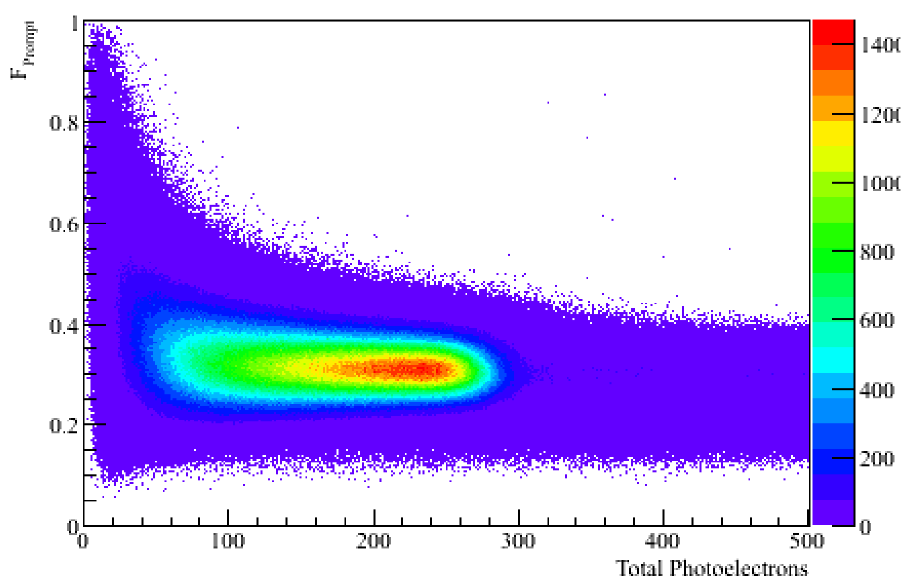

Figure 4.5: Total ^{22}Na gamma calibration population

The neutron population used in this analysis contains approximately 4000 neutron events [61], shown in Figure 4.6 with $F_{Prompt} > 0.7$. These events were collected within a single run over a period of approximately 70 hours. Note the population at F_{Prompt} ~0.3, is due to the gamma event following many of the (α,n) Am-Be events as well as those from background, as the source is not tagged.

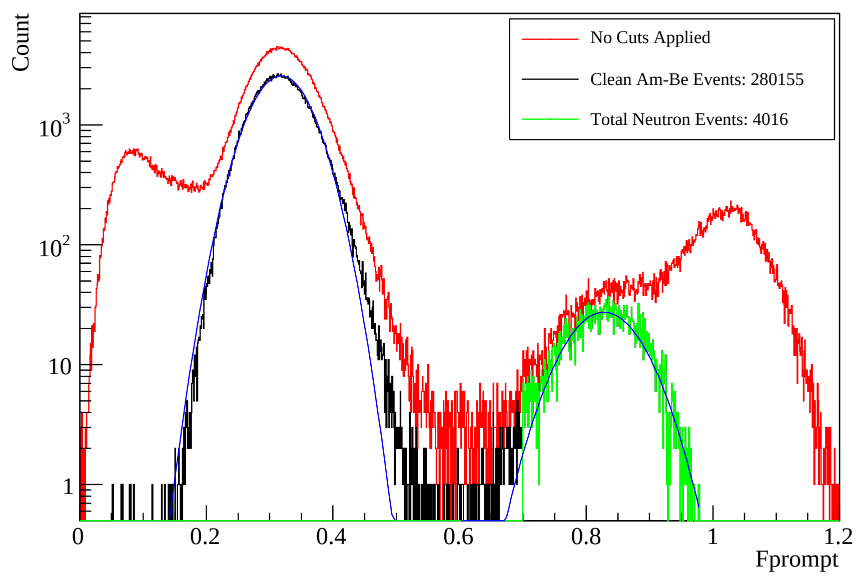

Figure 4.6: ^{241}Am-^{9}Be gamma and neutron population

Note the separation of the gamma and neutron populations in Figure 4.6. As the annulus was not used in tagging Am-Be events, a higher rate of background events is expected than in Na-22 calibration. Furthermore, the data cleaning cuts, discussed in the next section, were relaxed here to leave a statistically significant number of neutron events for calibration. The total F_{Prompt} Am-Be population up to 500 photoelectrons is shown in Figure 4.7.

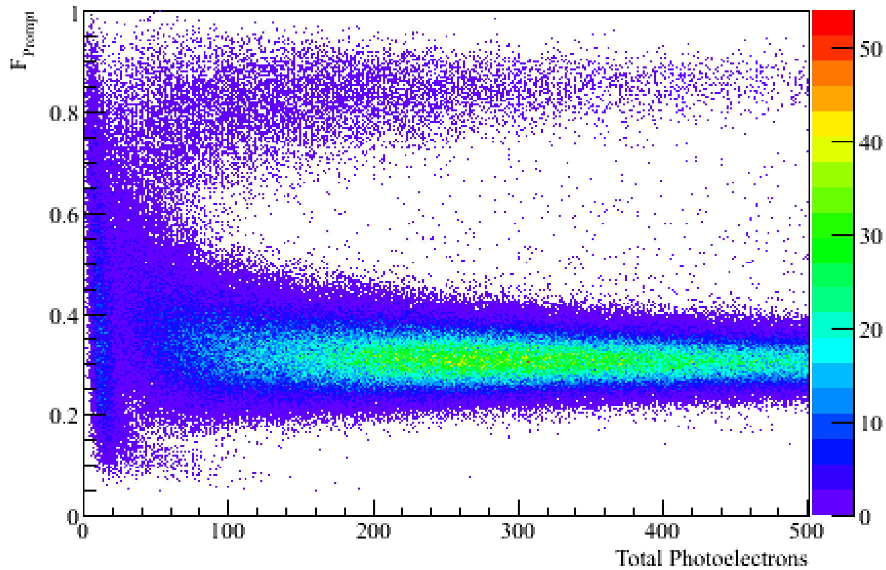

Figure 4.7: Total ^{241}Am-^{9}Be event population, F_{Prompt} distribution over energy

The top band corresponds to nuclear recoil events, the bottom band corresponds to γ and β events.

4.2 Data Processing

A set of procedures were applied to each data run to convert raw oscilloscope traces into numbers of photoelectrons, and to create a set of useful properties for analysis, such as the F_{Prompt} value and position, for each scintillation event.

4.2.1 Baseline Correction

An event by event baseline correction is applied in software, to correct for any systematic shift of the detector response over energy. This is achieved by fitting a linear function to 500 ns of data before the trigger time for each event, and similarly to the remaining 5 microseconds of data, after signal information has been removed.

The voltage correction, in units of Volts, is typically on the order of,

$$V_{new} = 2.56\times10^{-4} + \left(1.3\times10^{-7}\right)\cdot V_{old}$$

The effect of the baseline correction on the energy distribution is shown in Figure 4.8, where the energy axis is plotted in the number of photoelectrons. Note the shift and increased resolution of the 511 keV energy peak.

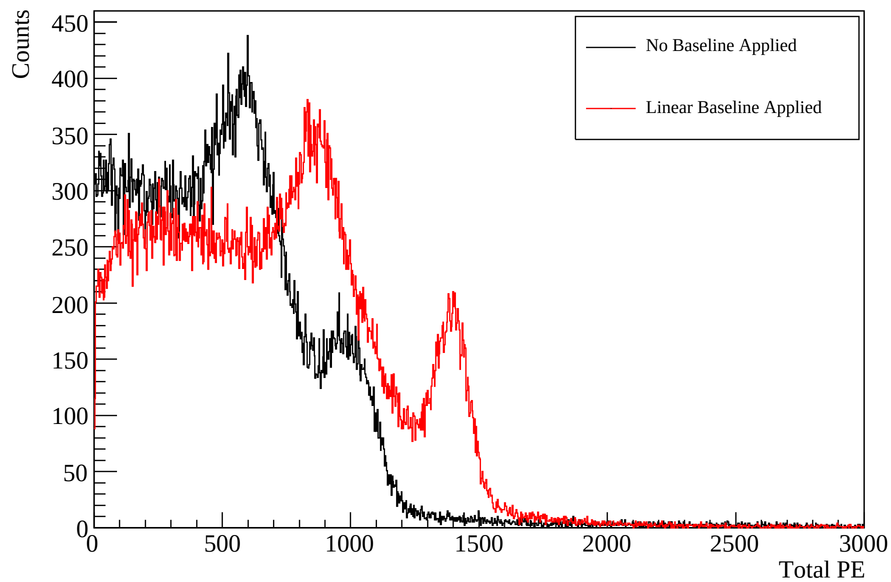

Figure 4.8: Energy spectrum with baseline and no applied baseline

4.2.2 Single Photoelectron Calibration

An event is defined as the population of scintillation photons detected within 10 microseconds, the first hundred nanoseconds of which is dominated by the prompt scintillation light.

A large prompt peak is seen in the raw spectrum, as shown in Figure 4.1, due to pileup of the prompt scintillation events, having been produced primarily from the singlet dimer, with a lifetime of only 7 ns (see section 2.1.2). This peak is integrated and converted to photoelectron number by a single photoelectron (SPE) calibration.

In order to calibrate the voltage integral to photoelectron number, we seek peaks produced by single photoelectrons. As the mean lifetime of the triplet state is 1.6 μs, the late scintillation decays away over many microseconds. We expect isolated peaks late in the voltage trace to be due to single photoelectrons. The area of these peaks was used to determine the SPE calibration. The distribution of the integrated area for many single photoelectron events is shown in Figure 4.9, for a single Na-22 gamma calibration run 48 hours long.

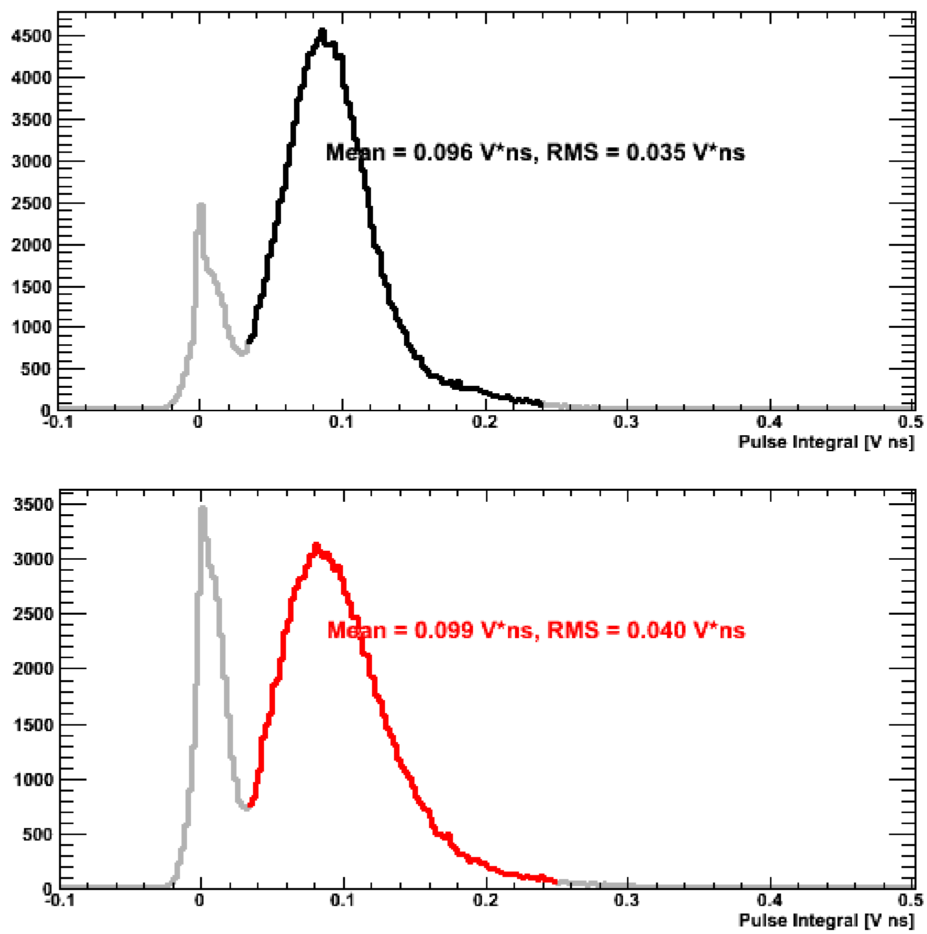

Figure 4.9: Single photoelectron spectrum
PMT A (top) and PMT B (bottom) (run #523)

Signals larger than a chosen threshold, of larger than 5 mV were integrated. The leading peak seen in Figure 4.9 is due to the integration of noise larger than the chosen threshold. The second peak is the distribution of the integrated area of single photoelectrons, the fit of which determines the SPE calibration. The SPE distribution was fit for each data run, for the SPEs detected by each PMT. The calibration used here, (found for run #523) is,

$$\begin{aligned}\mu_{\mathrm{SPE}} \pm \sigma_{\mathrm{SPE}} &= \frac{\mu_{\mathrm{SPE,A}} + \mu_{\mathrm{SPE,B}}}{2} \pm \frac{\sqrt{\sigma^2_{\mathrm{SPE,A}} + \sigma^2_{\mathrm{SPE,B}}}}{2} \\ &= 0.098 \pm 0.027\ \mathrm{V \cdot ns}\end{aligned} \tag{4.2}$$

where A and B refer to each of the detector PMTs.

4.2.3 Systematic Data Cleaning

The processed data is "cleaned" of events which are assumed to be triggered by noise, background or due to effects such as pileup, by a selected set of systematic cuts.

4.2.3.1 Position

As the construction materials are a potential source of background events, it is desired to remove those events which originate in a region near the surfaces. As a PMT was located at either end of the chamber, an approximate position in the dimension along the chamber can be calculated by taking the ratio of the total light signal collected in each PMT. A position parameter (in cm) was assigned to each event, based on the position relative to the centre, spanning the chamber and including the light-guides. This position parameter, here named Z_{fit}, is written as,

$$Z_{\mathrm{fit}} = \frac{\mathrm{TotalPE_A}\left(-35.2\mathrm{cm}\right) - \mathrm{TotalPE}_B\left(35.2\mathrm{cm}\right)}{\mathrm{TotalPE_A} + \mathrm{TotalPE}_B} \tag{4.3}$$

where TotalPE is the total number of photoelectrons as detected by each PMT and the lengths represent the length to the PMTs (the length of the chamber plus length of the light-guide).

For Na-22 calibration, an event having a position of less than or greater than 10.0 cm from the centre was cut. This was done event by event, by first finding the mean of the position distribution for each run, and correcting for any asymmetry if present.

Most tagged Na-22 events lie within the 10 cm, though it was observed a large fraction of the background (discussed in section 4.6) is generated at larger Z_{fit}, at positions within the light-guides, suspected to be Cherenkov radiation produced by muons in the acrylic.

4.2.3.2 PMT Coincidence Data Cut

The scintillation light from a single event is required to be detected in both PMTs simultaneously. In practice this is achieved by setting a very short time interval in which both PMTs trigger. This is done initially in hardware. In the processed data, the interval is set to 40 ns.

4.2.3.3 Positive Prompt & Late Light Components

As some events may have been triggered with very little light, hence events are cut which, after processing, have a negative (or zero) late or prompt component.

4.2.3.4 PMT Trigger Time

Events having a difference of less than 20 ns of the edge times between the two PMTs were cut. In addition, for each run the trigger time of each event is histogrammed and the peak is calculated by fitting a Gaussian. Events are cut when arriving more than 30 ns earlier or later than the mean trigger time.

4.2.3.5 Pile-up Events

The pile-up of events is reduced in the signal electronics, as discussed in section 3.2, though some events are observed in the recorded data. Events with any sign of pile-up were cut.

4.2.4 Cut Efficiencies

Here we investigate the efficiency of different cuts to the data. Figure 4.10 shows the fraction of events remaining bin by bin, for a specific cut relative to the number of events if no cuts were applied. We see for events with photoelectron number of less than 100, significantly more events are being removed by each cut.

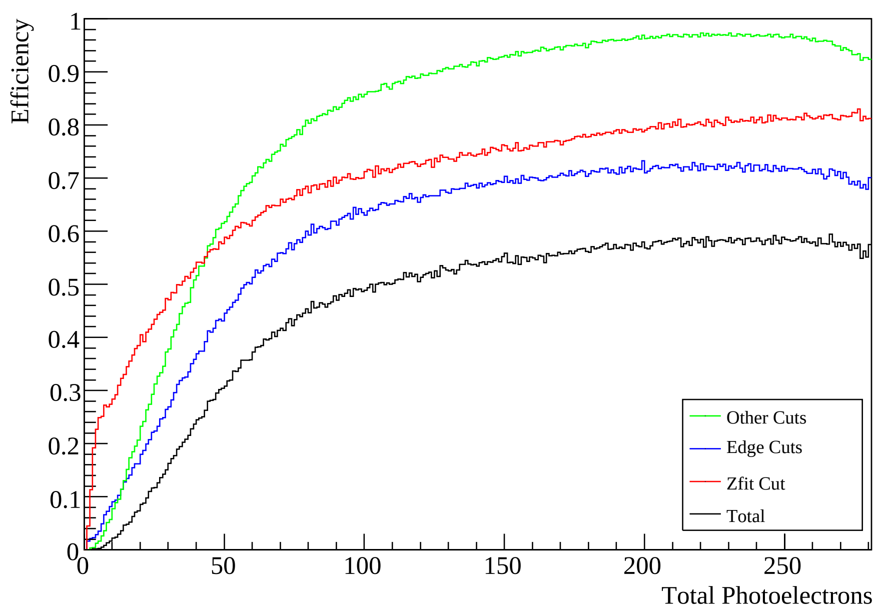

Figure 4.10 Cut efficiency up to 300 photoelectrons

4.3 Energy Calibration

The energy calibration of the detector was routinely measured using the Na-22 source tagged by the annulus, and a source of Ba-133, to characterise the detector over a range of energy.

The decay of Ba-133 produces the gamma rays listed in Table 4.1. Of these, the 81 keV and 356 keV gammas were used, being the more intense of the emitted gammas. The observed low energy peak from barium will be a sum of the 81 keV gamma and the less intense 80 keV gamma.

E (keV)	I (%)
53.2	2.2
79.6	2.6
81.0	34
276.4	7.2
302.9	18
356.0	62
383.9	8.9

Table 4.1: Gamma rays from ^{133}Ba [53]

4.3.1 Energy Spectrum

The energy spectrum for the Na-22 and Ba-133 sources is shown in Figure 4.11. The peaks were fit with a Gaussian function, the parameters of which are summarised in Table 4.2.

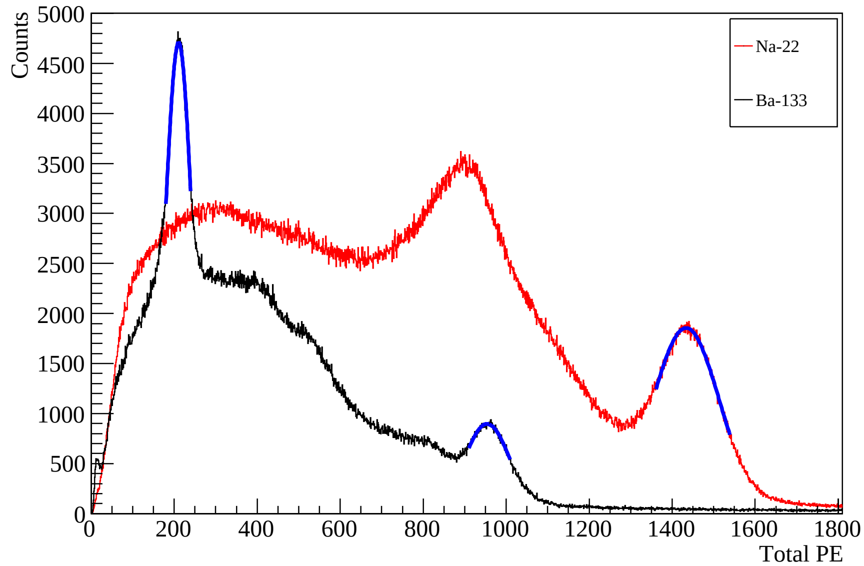

Figure 4.11: Energy spectrum for Na-22 and Ba-133

The uncertainty on each peak in Table 4.2, is the combination of the uncertainty in the fit, the uncertainty in the single photoelectron calibration (see section 4.2.2) and the statistical uncertainty, given by,

$$\begin{aligned}\sigma_{\text{Peak}}{}^2 &= \sigma^2_{\text{Fit}} + \sigma^2_{\text{SPE Calibration}} + \sigma^2_{\text{Statistical}} \\ &= \sigma^2_{\text{Fit}} + \frac{\sigma^2_{\text{SPE Dist.}}}{\mu^2_{\text{SPE Dist.}}}\mu_{\text{Peak}} + \mu_{\text{Peak}}\end{aligned} \tag{4.4}$$

where $\sigma_{\text{Statistical}} = \sqrt{N_{\text{PE}}} = \sqrt{\mu_{\text{Peak}}}$ and the SPE distribution has been normalised to one SPE.

	Peak	Width	χ^2/ndf	Photoelectrons/keV
^{22}Na 511 keV	1433 ± 38	80.8 ± 0.5	183/177	2.80 ± 0.07
^{133}Ba 356 keV	954 ± 31	54.9 ± 0.8	75/97	2.68 ± 0.09
^{133}Ba 81 keV	211 ± 15	33.3 ± 0.3	79/57	2.60 ± 0.18

Table 4.2: Energy calibration peaks (Gaussian fits)

Note the large Compton edge of the 511 keV Na-22 gamma and the ratio of the observed peaks in barium compared with their given intensities in Table 4.1. Only a fraction of the total 356 keV gammas contribute their full energy to the peak. Additionally, since the spectrum is shown after data cleaning cuts, we can estimate from Figure 4.10, that an additional 10% of events are being removed from the 80 keV peak than the 356 keV peak.

4.3.2 Energy Linearity

Following the results of the energy calibration, it was desired to investigate the linearity of the detector response with energy. The data is shown in Figure 4.12, for the 511 keV Na-22 and the Ba-133 fit peaks. The intercept is consistent with zero as would be expected.

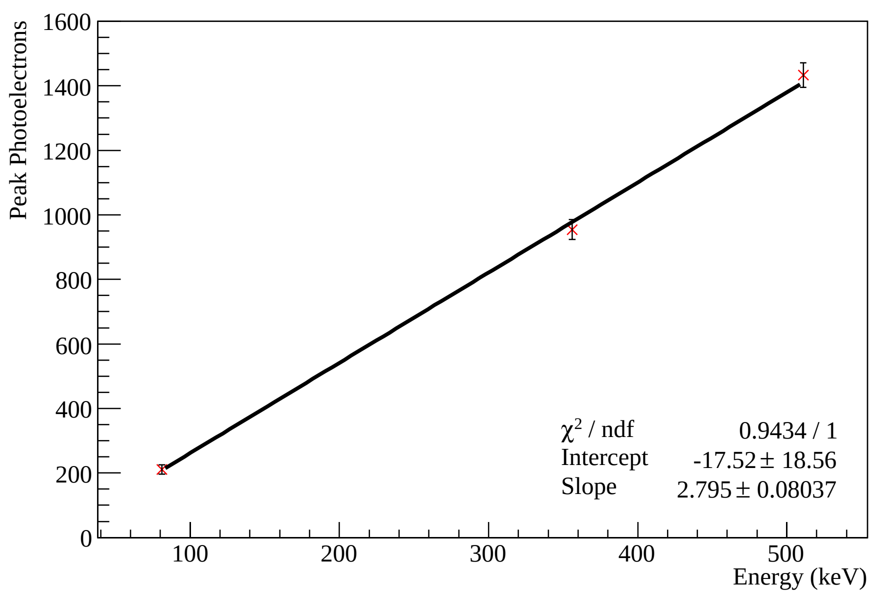

Figure 4.12: Energy calibration based on Na-22 and Ba-133 peaks

The light yield was calculated for each peak, shown plotted with energy in Figure 4.13. The light yields are consistent within the uncertainty, where the intercept on the fit slope is consistent with fitting a straight line through the points. Furthermore, the stability of the yield indicates the detectors stability over time, as the barium data was record early in the detectors operation, whereas the Na-22 data were taken routinely over the span of the operational time. This will be discussed further in the next section.

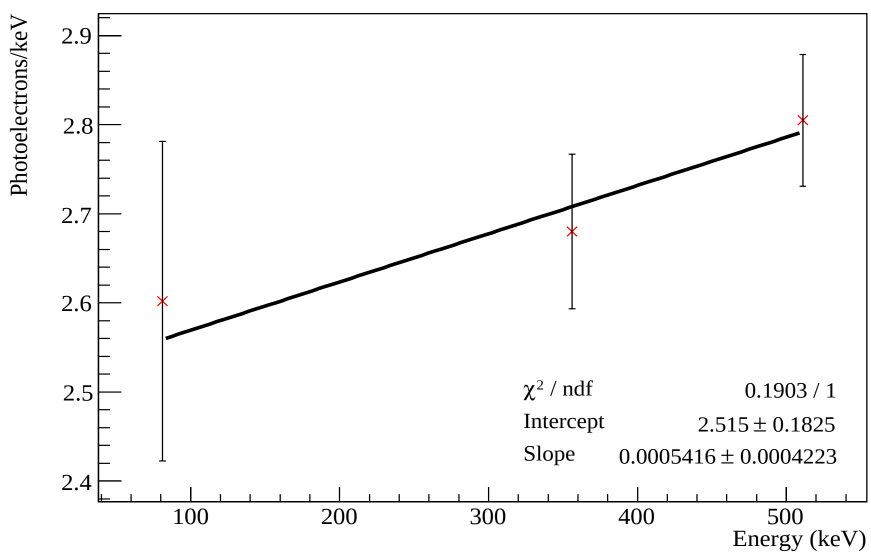

Figure 4.13: Light yield dependency on photoelectron number

4.3.3 Energy Stability

The routine energy calibration, over the 2 month period the detector was operational, provided a measurement of the detectors stability. Figure 4.14 plots the calibrated light yield for each of the Na-22 runs over this period, given the data in Table 4.2.

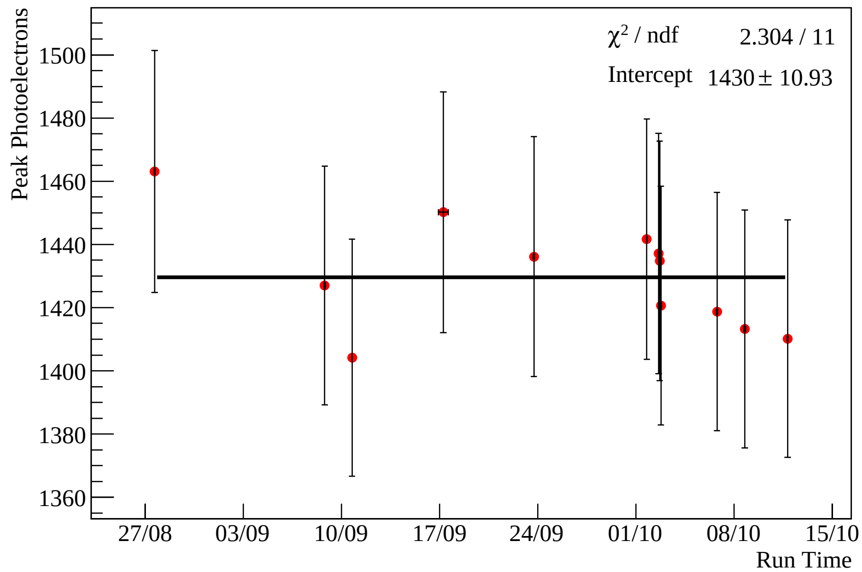

Figure 4.14 Light yield time dependence.

The stability of the detector is dependent on the purity of the argon. If impurities were present they would absorb energy from excited triplet states, increasing the rate of non-radiative transitions of the triplets (see section 2.1), quenching the late scintillation light. This would lead to a variation in the energy calibration, the mean of the F_{Prompt} distribution and the observed triplet lifetime (discussed in section 4.4). The stability of the F_{Prompt} distribution over the operational time is shown in Figure 4.15. To find the peak, the population was roughly fit with a Gaussian (section 5.1 discusses a more correct, analytical fit).

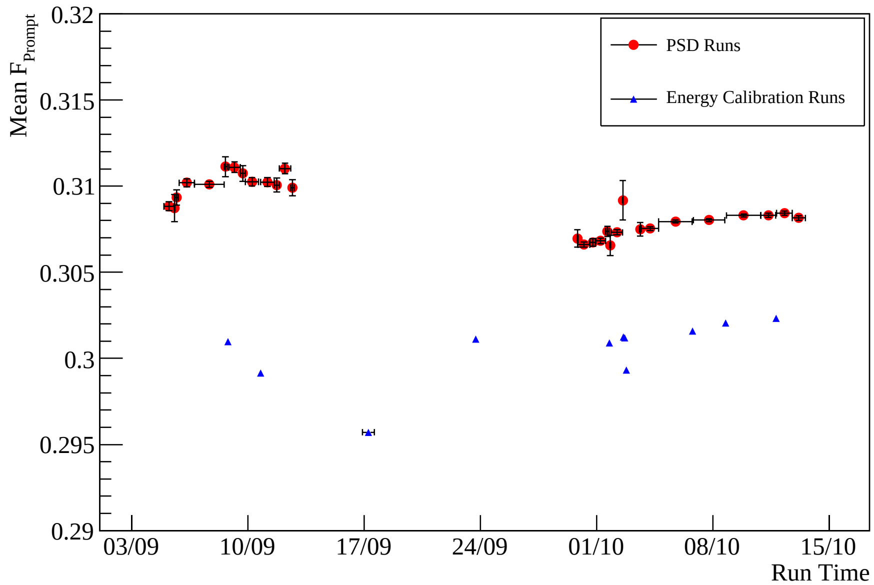

Figure 4.15: F_{Prompt} dependence on time

The observed difference between the F_{Prompt} mean for the PSD and energy calibration runs, as seen in Figure 4.15, is due to the removal of high energy events by the SCA (see section 3.1.11). For PSD running, higher energy events are not of interest, and those with more than 300 photoelectrons are cut. The mean F_{Prompt} shifts lower due to the high number of background events of fewer than 100 photoelectrons.

4.4 Measurement of the Triplet Lifetime

A measurement was made of the lifetime of the triplet states, by summing traces and fitting 3 microseconds in the tail of the total PMT charge, shown in Figure 4.16. The measured lifetime was found to be 1528 ± 98 ns, where the uncertainty is the standard deviation of the fit lifetimes, shown in Figure 4.17, added in quadrature with the uncertainty of each point to account for the uncertainty in each fit. This lifetime is consistent with measurements made by the miniCLEAN detector [21]. The late lifetime was found to be stable over the period the detector was in operation, shown in Figure 4.17.

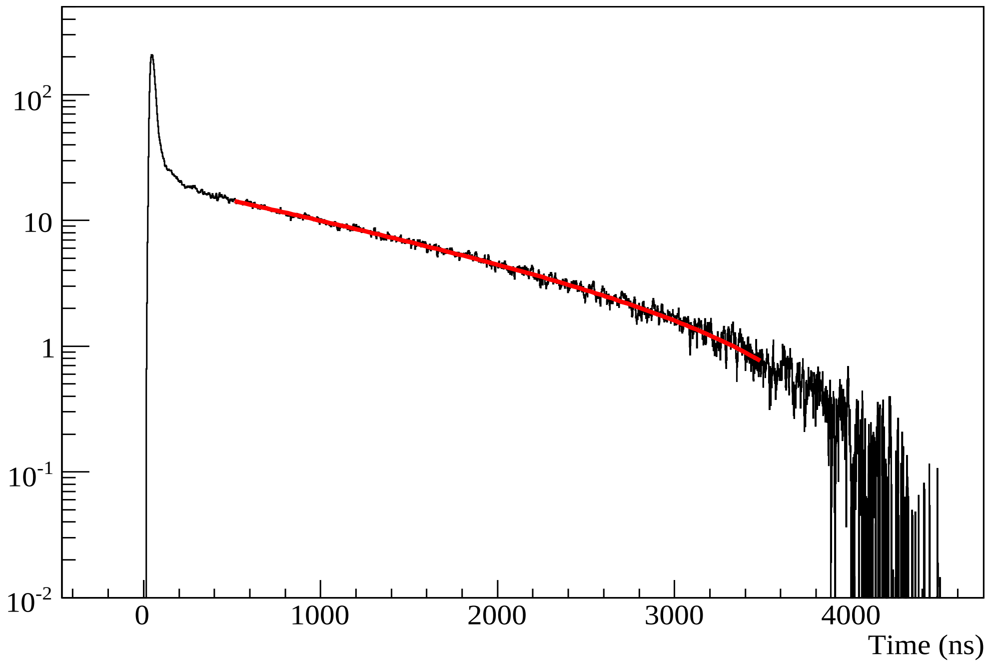

Figure 4.16: Measurement of the triplet lifetime
run #445 with τ = (1518 ± 65) ns

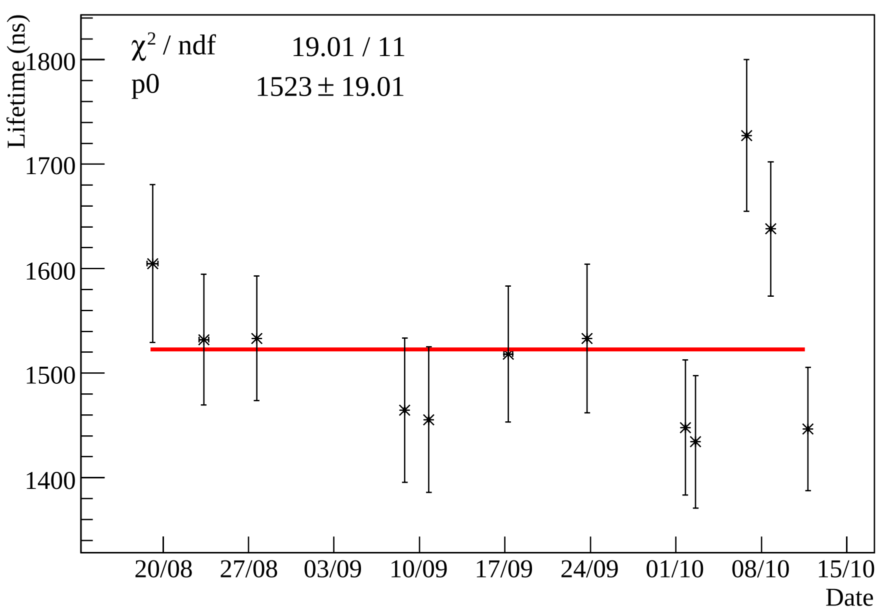

Figure 4.17: Stability of the measured triplet lifetime

4.5 Prompt and Late Noise

Measurements of the electronic noise were obtained by triggering the data acquisition electronics using a random pulse generator. The detector response within the prompt and late windows is shown in Figure 4.18, each fit with a Gaussian function. This component of noise is representative of the noise generated by the hardware electronics, and analysis algorithms.

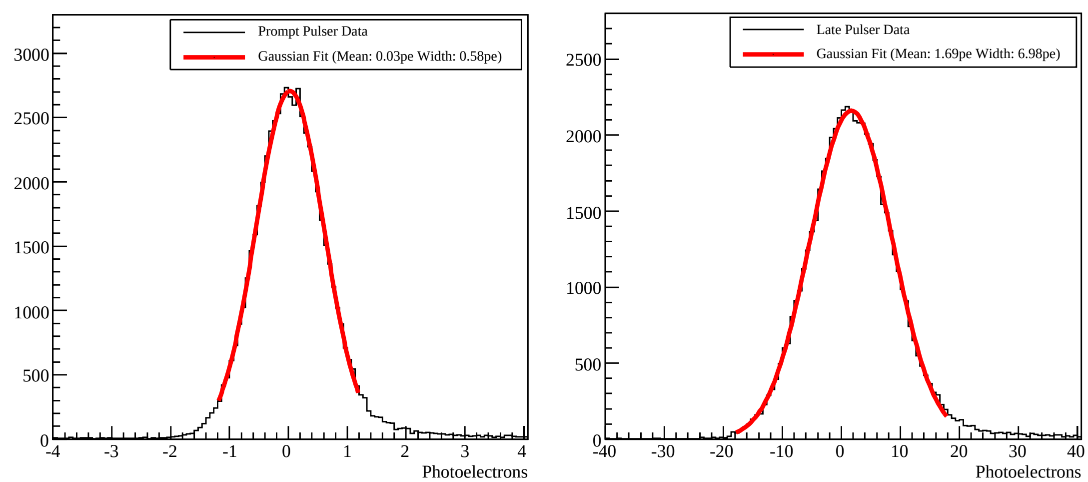

Figure 4.18: Random pulser noise components

Note the change of scale in the x-axis

The late light, integrated over a window of 10 μs is more susceptible to electrical noise than the short, prompt window, 150 ns wide, indicated in Figure 4.18.

The prompt and late noise components were found to be highly correlated, shown in Figure 4.19.

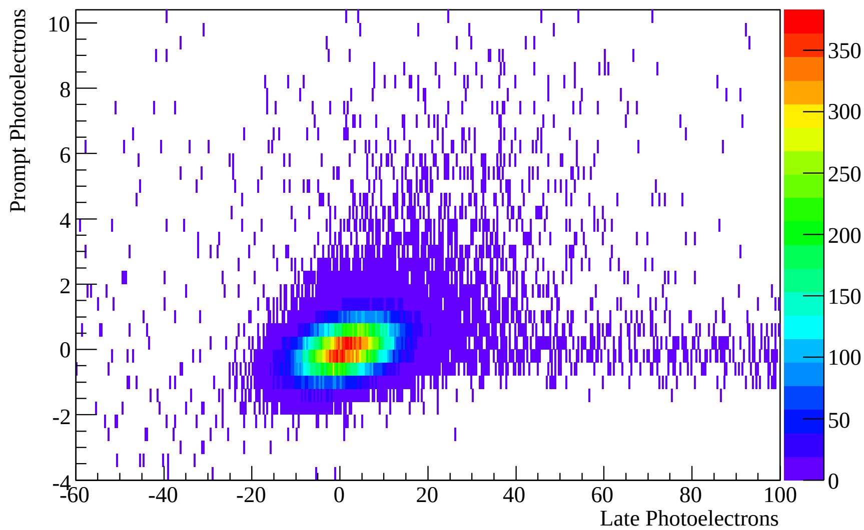

Figure 4.19: Prompt & late noise correlation of random pulser data

When calculating the ratio of prompt to total light, a significant amount of the correlated portion of the uncertainty will cancel, hence only the uncorrelated portion of electrical noise will contribute to the uncertainty on F_{Prompt}. Here we estimate the uncorrelated portion of the late noise, given the prompt component is small, assuming the uncertainty in the late to prompt fraction is given by,

$$\begin{aligned}\left(\frac{\sigma_{L/P}}{\mu_{L/P}}\right)^2 &= \left(\frac{\sigma_L}{\mu_L}\right)^2 + \left(\frac{\sigma_P}{\mu_P}\right)^2 + \frac{2\sigma_L\sigma_P\rho_{LP}}{\mu_{L/P}} \\ &\simeq \left(\frac{\sigma_L}{\mu_L}\right)^2 \\ \therefore \quad \sigma_L &\simeq \frac{\sigma_{L/P}}{\mu_{L/P}}\mu_L\end{aligned} \tag{4.5}$$

The fractional uncertainty in the late to prompt ratio was found using a Gaussian fit to the pulser data, as shown in Figure 4.20. The fit is not ideal, as indicated by the χ^2 parameter, and is subject to fitting systematics. Further work on the reduction of electrical noise would be beneficial in understanding and reducing this noise component.

Using these parameters and the late mean from Figure 4.18 we estimate the uncorrelated portion of the late electrical noise to be 3.7 photoelectrons.

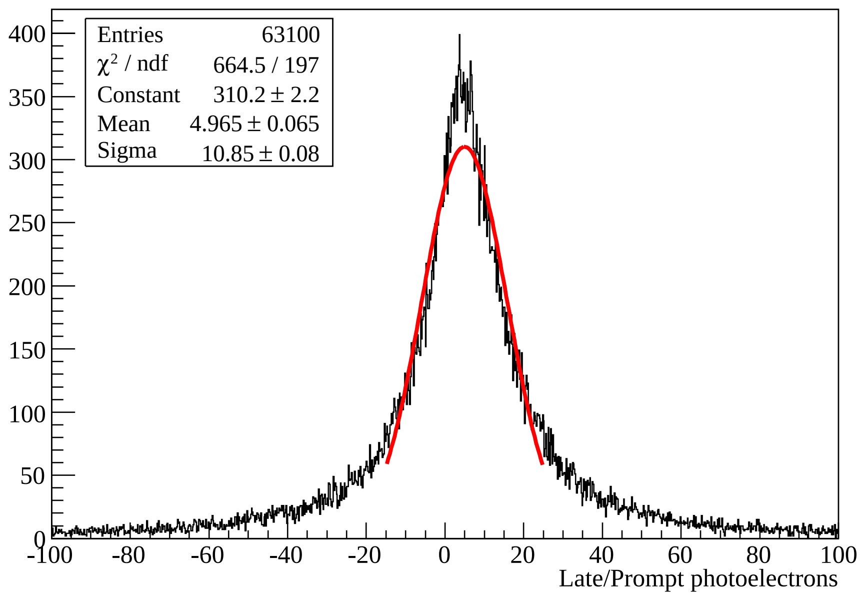

Figure 4.20: Late to prompt random pulser distribution

4.6 Background

Routine background measurements were made over the time the detector was operational. A total of 8.0 days (2.7 days livetime) of background data were recorded, dispersed throughout the period calibration data were collected.

The spectrum of background events is shown in Figure 4.21. Sources of background were discussed in section 2.2. A wide spectrum of low F_{Prompt} events (~0.3) are due to local beta and gamma sources, including the beta decays of argon-39. Here we are concerned with background events within the region of interest for a WIMP search. These events lie in the chosen energy region of interest, highlighted in Figure 4.21, of 120 – 240 photoelectrons, and are neutron-like, high F_{Prompt} events. The expected sources of high F_{Prompt} events are those from the radioactive impurities in the detector materials, radon contamination of surfaces and cosmic ray events, of which the cosmogenic background will be the primary source of high F_{Prompt} events while on surface. The cosmogenic background and its reduction underground were discussed in section 2.2.2.3.

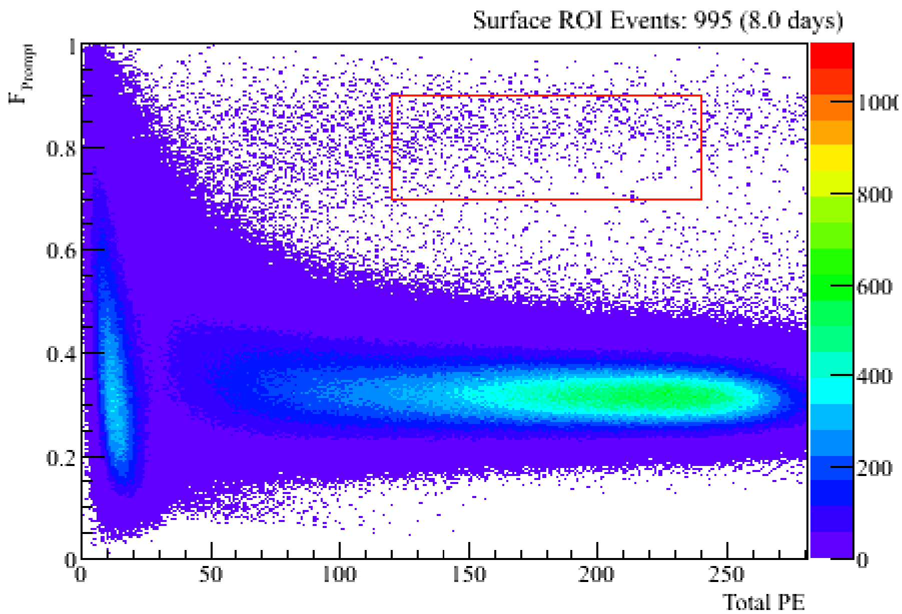

Figure 4.21: F_{Prompt} distribution of background events region of interest boxed in red

In order to properly measure the background rate it was necessary to understand the detector live-time.

The detector live-time is dependent on the speed of which the data acquisition (DAQ) system can record data (measured in real seconds at approximately 20 events/s). The corrected rate is the product of the DAQ throughput and the actual trigger rate. The live-time is then the actual time span of the run divided by the corrected trigger rate, simply,

$$\text{livetime} = \frac{\text{real time} \times \text{DAQ throughput}}{\text{trigger rate}}$$
$$\text{background rate} = \text{background events} \,/\, \text{livetime} \tag{4.6}$$

In the current configuration for recording background, the live-time was found to be approximately 30% of the real time. (For Na-22 PSD calibration, this number is as high as 80%, due to the slower trigger rate of the multiple-coincidence with the annulus.)

The background rate for events of 120 - 240 photoelectrons with $0.7 < F_{Prompt} < 0.9$ is shown in Figure 4.22. The rate was found to be 3.71 ± 0.13 mHz and constant over the operational period of the detector.

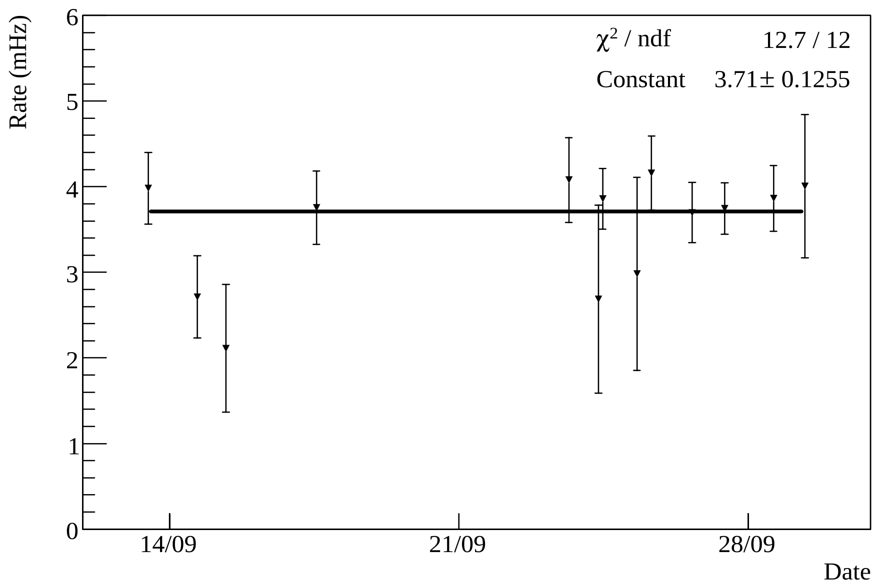

Figure 4.22: Stability of detector background

The position distribution of the background events within the detector is shown in Figure 4.23. As discussed in section 4.2.3.1, events were cut ±10 cm from the centre, after correcting for any asymmetry (due to a difference in PMT gain).

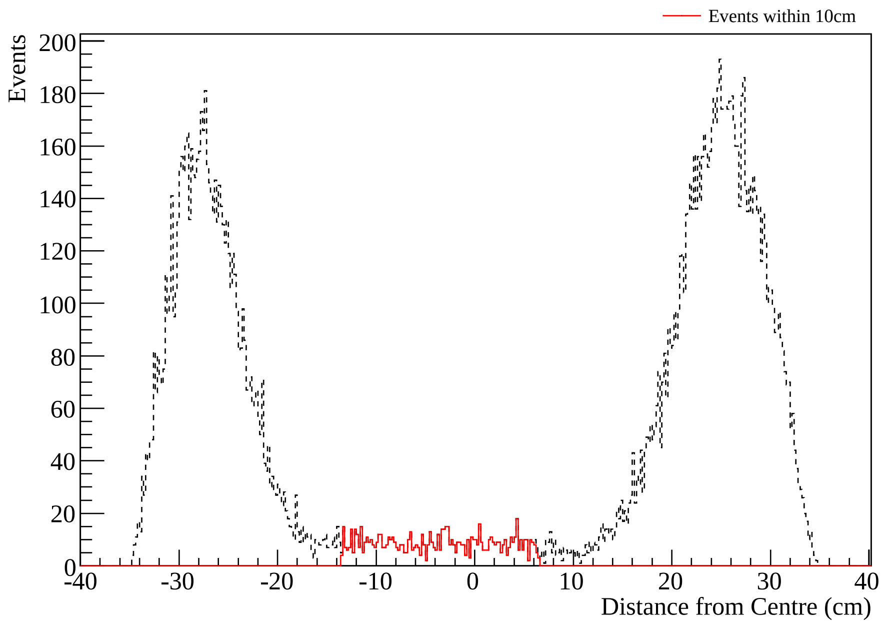

Figure 4.23: Position distribution of background in the region of interest

By relaxing the cut on position, we see increased numbers of events beyond 10 cm, toward either end of the detector (see position cut description 4.2.3.1) as shown in Figure 4.23.

The peaks seen in Figure 4.23 correspond to a position near the centre of the light-guides. These events are likely due to high-energy through-going muons producing Cherenkov radiation when passing the light-guides. High F_{Prompt} events could also be due to muon spallation in the detector materials and surrounding material. This background, being due to cosmic muons, is reduced when operating underground.

It is also possible high F_{Prompt} events could also be produced by the radon contamination of surfaces or the decay of radioactive impurities in the argon chamber and the photomultipliers, though the rate of these, discussed in section 2.2.2.1, is expected to be lower.

The background events seen in the centre of the detector, as seen in Figure 4.23, are likely long-lived events from the tails of the cut events. The F_{Prompt} distribution of the background events was shown in Figure 4.21.

4.6.1 Initial Underground Background Data

Since moving the detector underground to SNOLAB, preliminary background runs have been recorded. Preliminary investigation have indicated that the rate of events in the region of interest to be a factor of 20 lower (taking into account livetime) than on surface. Figure 4.24 shows the spectrum of these F_{Prompt} events, with the region of interest highlighted.

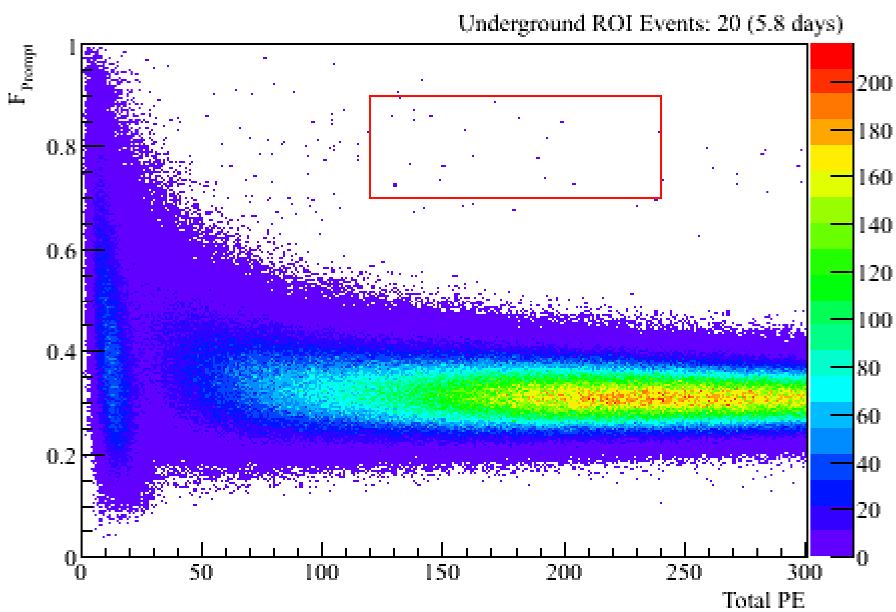

Figure 4.24: Preliminary underground background data

One modification that was made to the detector when moving underground was the replacement of the light-guides. New light-guides were fabricated from plain cast acrylic, without the UV absorber present in the light-guides used on surface. It was known that the spectrum of light attenuated by the UV absorber continued up to 440 nm. Since the cosmic background underground is lower, plain acrylic was used in hope of increasing the light yield. Figure 4.25 shows the comparison of the distribution of backgrounds on surface and underground.

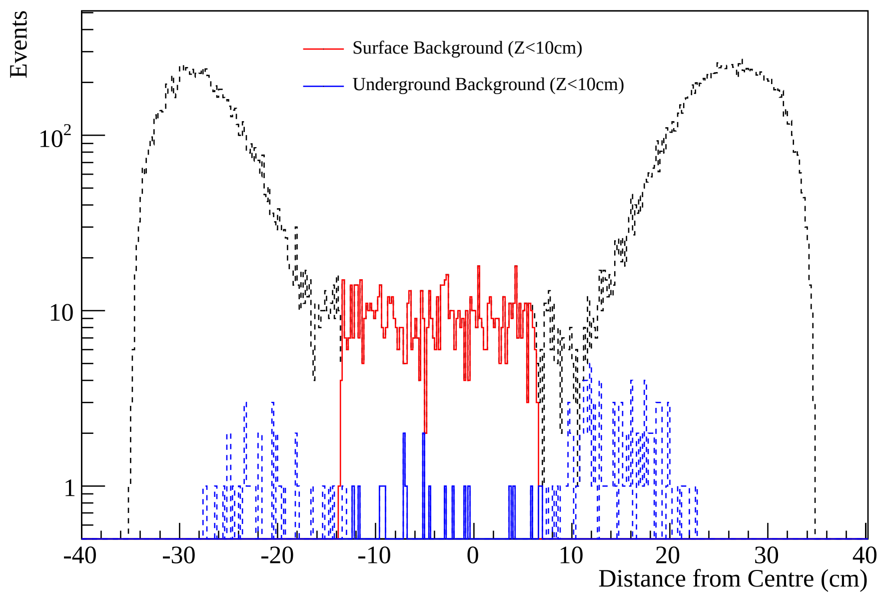

Figure 4.25: Observed background on surface, underground (in Z)

The events localised in the light-guides, as seen in the surface background, and discussed previously, have been drastically reduced when moving the detector underground, indicating that the events were due to cosmic muons. The underground background events, shown in Figure 4.25, though low in statistics, are located closer to the argon chamber. These events may be due to radon contamination of the surfaces.

Chapter 5

Pulse Shape Discrimination

In the previous chapters we have given an overview of the detector itself, investigating scintillation properties, its measured characteristics and its stability. In this chapter we seek to demonstrate the feasibility to discriminate all background by use of pulse shape analysis in order for this technology to be used in a sensitive dark matter search.

5.1 An Analytic Model for PSD

With data on the pulse shape discrimination in the DEAP-1 detector, we wish to model the processes which determine the discrimination and project the discrimination level that would be achievable in a more massive detector. The limits from DEAP-1 are those presented by using a small mass of argon, and those by the cosmogenic background that is unavoidable when the detector is on the Earth's surface.

We begin by modelling the distribution of the F_{Prompt} statistic. We assume the prompt and late components of the light to be independent and random processes, based on each being populated by the scintillation light produced in the de-excitation of singlet and triplet states. Being normally distributed, each component has a given mean and variance. We restate the fraction of prompt to total light as,

$$\begin{aligned} F_{\mathrm{Prompt}} &= \frac{f_{\mathrm{P}}}{f_{\mathrm{P}} + f_{\mathrm{L}}} \\ &= \frac{1}{1+\dfrac{f_{\mathrm{L}}}{f_{\mathrm{P}}}} \end{aligned} \tag{5.1}$$

where f_P and f_L are the prompt and late fractions of total light.

Their ratio can be modelled by a probability function formed by the ratio of two distribution functions, each one for a normally distributed variable, in the manner reported by Hinkley [63]. The function is given by,

$$\begin{aligned} f(w) = &\frac{b(w)d(w)}{\sqrt{2\pi}\sigma_1\sigma_2 a^3(w)}\left[\Phi\left\{\frac{b(w)}{\sqrt{(1-\rho^2)}a(w)}\right\} - \Phi\left\{-\frac{b(w)}{\sqrt{(1-\rho^2)}a(w)}\right\}\right] \\ &+ \frac{\sqrt{1-\rho^2}}{\pi\sigma_1\sigma_2 a^2(w)}\exp\left\{-\frac{c}{2(1-\rho^2)}\right\} \end{aligned} \tag{5.2}$$

where,

$$a(w) = \left(\frac{w^2}{\sigma_1^{\,2}} - \frac{2\rho w}{\sigma_1\sigma_2} + \frac{1}{\sigma_2^{\,2}}\right)^{\frac{1}{2}},$$

$$b(w) = \frac{\theta_1 w}{\sigma_1^{\,2}} - \frac{\rho(\theta_1 + \theta_1 w)}{\sigma_1\sigma_2} + \frac{\theta_2}{\sigma_2^{\,2}}$$

$$c(w) = \frac{\theta_1}{\sigma_1^{\;2}} - \frac{2\rho\theta_1\theta_1}{\sigma_1\sigma_2} + \frac{\theta_2}{\sigma_2^{\;2}}$$

$$d(w) = \exp\left\{\frac{b^2(w) - ca^2(w)}{2(1-\rho^2)a^2(w)}\right\}.$$

and $\Phi(y) = \int_{-\infty}^{y} \phi(u)\,du$, where $\phi(u) = \frac{1}{\sqrt{2\pi}} e^{-\frac{1}{2}u^2}$.

In our case we assume no correlation in the prompt and late scintillation due to the scintillation being produced from singlet and triplet states independently, and set the correlation parameter, ρ, to zero. Though the full function was used in analysis, if we approximate that the terms including the Φ function and the last exponential term are sufficiently close to unity, this function approximates to a simpler form easier to visualise,

$$P\left(\mu_{\mathrm{P}}, \mu_{\mathrm{L}}, \sigma_{\mathrm{P}}^2, \sigma_{\mathrm{L}}^2; w\right) = \frac{1}{\sqrt{2\pi}} \frac{\sigma_{\mathrm{L}}^2 \cdot \mu_{\mathrm{P}} + \sigma_{\mathrm{P}}^2 \cdot \mu_{\mathrm{L}} w}{\left(\sigma_{\mathrm{L}}^2 + \sigma_{\mathrm{P}}^2 w^2\right)^{3/2}} e^{-\frac{1}{2}(\mu_{\mathrm{L}} - \mu_{\mathrm{P}} w)^2 / \left(\sigma_L^2 + \sigma_{\mathrm{P}}^2 w^2\right)} \tag{5.3}$$

where μ is the mean and σ the width of the prompt and late distributions respectively. The distribution of events as predicted by the Hinkley formula is shown in Figure 5.1.

Equation (5.2) gives the probability for an event, typically made up of many hundred photoelectrons, being populated both by singlet and triplet states.

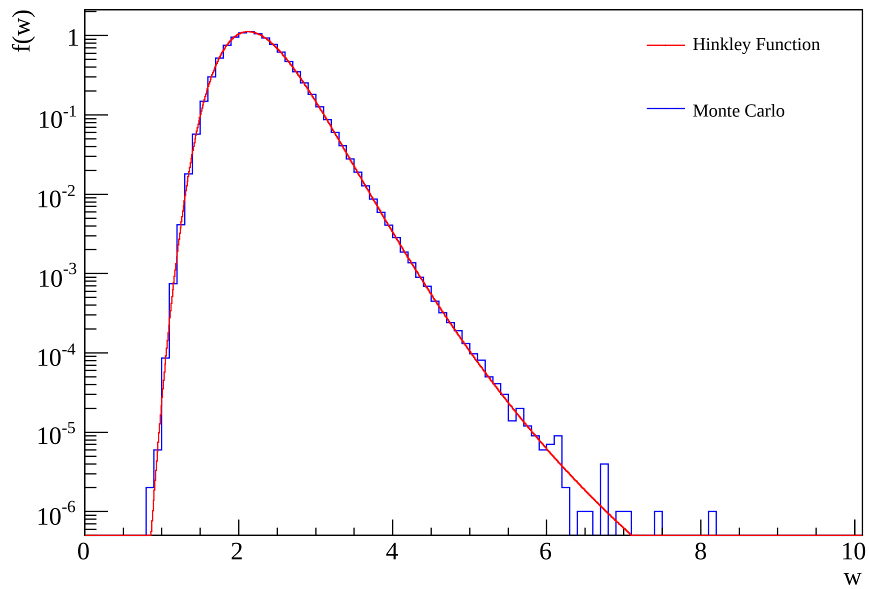

Figure 5.1: Probability distribution of the ratio of two normal, uncorrelated variables

5.1.1 Distribution Mean and Variance

The mean values of the prompt and late distributions of light are calculated given each events fraction of light, multiplied by the number of photoelectrons,

$$\begin{aligned} \mu_{\mathrm{P}} &= f_{\mathrm{P}} \cdot N_{\mathrm{PE}} \\ \mu_{\mathrm{L}} &= \left(1 - f_{\mathrm{P}}\right) \cdot N_{\mathrm{PE}} \end{aligned} \tag{5.4}$$

The fraction of prompt light measured for the Na-22 calibration population of proximately 31 million gamma events is shown in Figure 5.2 plotted against total photoelectron number. The nuclear recoil band, measured with approximately 4000 Am-Be neutron events is also shown. The bands are approximately flat over the energy range of interest, namely events of 120 – 240 photoelectrons.

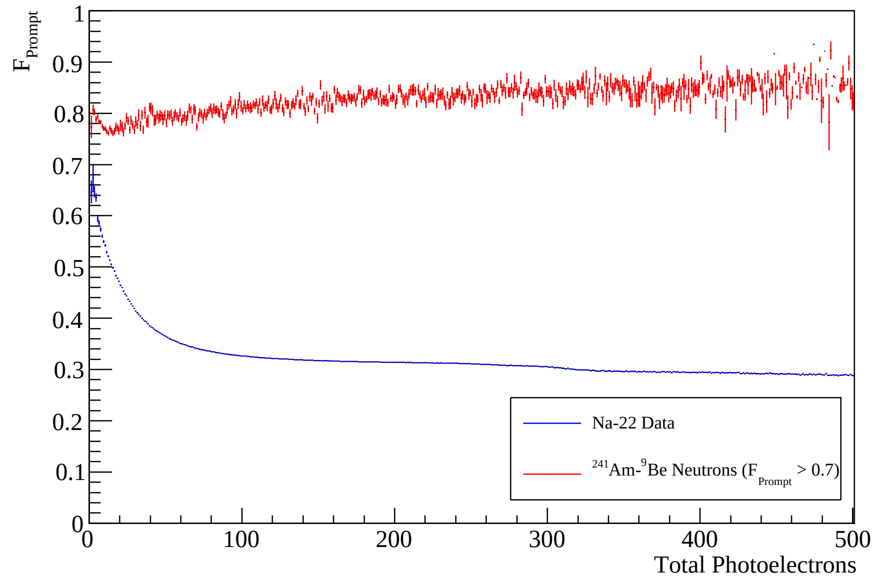

Figure 5.2: Measured fraction of prompt light for gamma and neutron events

In calculating the widths of the distributions, we first assume the total variance is a combination of the statistical uncertainty in counting the photoelectrons and the detector noise,

$$\sigma_{\mathrm{Total}}^2 = \sigma_{\mathrm{Statistical}}^2 + \sigma_{\mathrm{Noise}}{}^2 \tag{5.5}$$

For the prompt and late components, this is given by (assuming $\sigma_{\mathrm{Statistical}} = \sqrt{F \cdot N_{\mathrm{PE}}}$ where F is a Fano factor, though set to 1 throughout this analysis),

$$\begin{aligned} \sigma_{\mathrm{P}}{}^2 &= f_{\mathrm{P}} \cdot N_{\mathrm{PE}} + \sigma_{\mathrm{P}}^{\mathrm{Noise}\,2} \\ &= \left|\mu_{\mathrm{P}}\right| + \sigma_{\mathrm{P}}^{\mathrm{Noise}\,2} \\ \sigma_{\mathrm{L}}{}^2 &= \left(1 - f_{\mathrm{P}}\right) \cdot N_{\mathrm{PE}} + \sigma_{\mathrm{L}}^{\mathrm{Noise}\,2} \\ &= \left|\mu_{\mathrm{L}}\right| + \sigma_{\mathrm{L}}^{\mathrm{Noise}\,2} \end{aligned} \tag{5.6}$$

We model the components of noise as a sum of the uncertainty in the single photo-electron calibration, the electronic noise and the uncertainty in the counting window arising from the uncertainty in the trigger time,

$$\sigma^2_{\text{Noise}} = \sigma^2_{\text{SPE}} + \sigma^2_{\text{Electronic}} + \sigma^2_{\text{Window}} \tag{5.7}$$

During data processing, events with a trigger time larger than 30 ns than the mean trigger time were cut (see section 4.2.3.4). The waveform was shifted for events with a trigger time less than 30 ns of the mean, leading to an uncertainty in the late counting window and the counting of the late photoelectrons. This can be computed as,

$$\begin{aligned}\sigma_{\text{Window}} &= \frac{\int_0^{\Delta t} e^{-t/\tau} dt}{\int_0^{\infty} e^{-t/\tau} dt} \\ &= 1 - e^{-\Delta t/\tau} \\ &= 2.0\% \text{ late component}\end{aligned} \tag{5.8}$$

Using the measured single photoelectron noise (section 4.5), and the uncorrelated portion of the electronic noise found by the random pulser runs, the total noise equates to,

$$\begin{aligned}\sigma^2_{\text{P}} &= N_{\text{PromptPE}} + \left(\frac{\sigma_{\text{SPE}}}{\mu_{\text{SPE}}} \cdot \sqrt{N_{\text{PromptPE}}}\right)^2 + \sigma^2_{\text{PromptNoise}} + \sigma^2_{\text{Window}} \\ &= f_{\text{P}} \cdot N_{\text{PE}} + \left(\frac{0.027\text{pe}}{0.098\text{pe}} \cdot \sqrt{f_{\text{P}} \cdot N_{\text{PE}}}\right)^2 + (0.58\text{pe})^2 + (0.025\mu_{\text{L}})^2 \\ \sigma^2_{\text{L}} &= N_{\text{LatePE}} + \left(\frac{\sigma_{\text{SPE}}}{\mu_{\text{SPE}}} \cdot \sqrt{N_{\text{LatePE}}}\right)^2 + \sigma^2_{\text{LateNoise, Uncorrelated}} + \sigma^2_{\text{Window}} \\ \sigma^2_{\text{L}} &= (1 - f_{\text{L}}) \cdot N_{\text{pe}} + \left(\frac{0.027\text{pe}}{0.098\text{pe}} \cdot \sqrt{(1 - f_{\text{L}}) \cdot N_{\text{PE}}}\right)^2 + (3.7\text{pe})^2 + (0.025\mu_{\text{L}})^2\end{aligned} \tag{5.9}$$

The contribution of these components to the total noise over the range of total photoelectrons is shown in Figure 5.3 and 5.4.

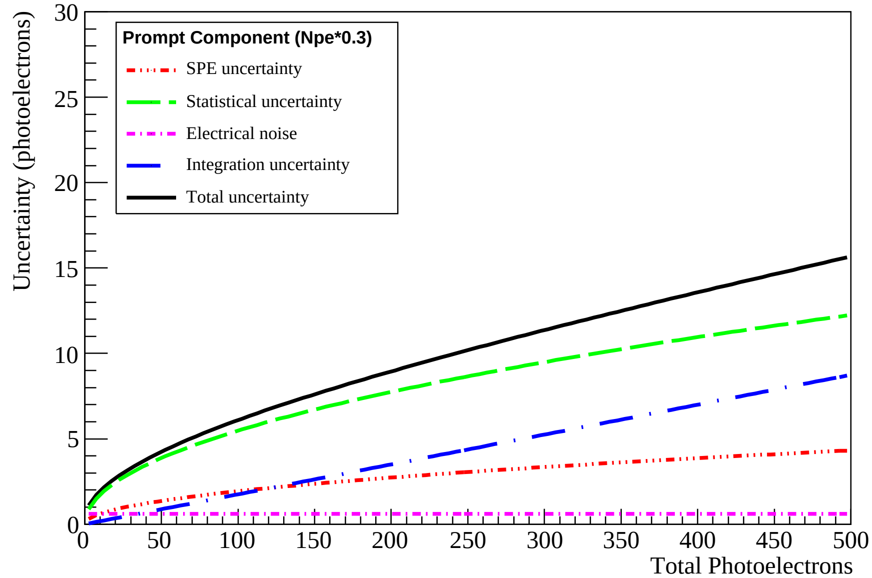

Figure 5.3: Prompt uncertainty components

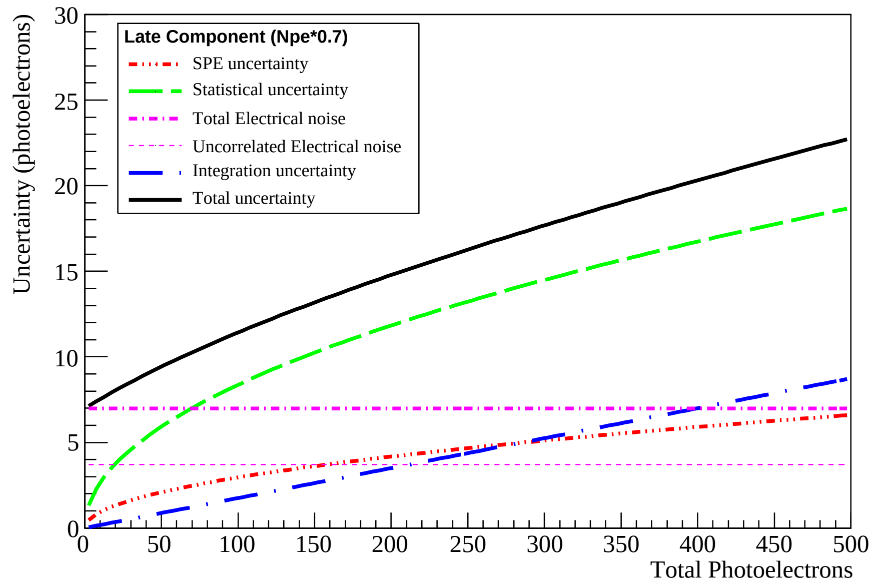

Figure 5.4: Late uncertainty components

The late signal suffers from a large electrical uncertainty, measured from the random pulser runs, however as discussed in section 4.5, when calculating the late to prompt ratio for F_{Prompt}, only the uncorrelated portion of the uncertainty remains, found to be approximately 3.7 photoelectrons.

We note after being dominated by the uncertainty in counting, the window and SPE uncertainties contribute to the total prompt and late by approximately 3 – 4 photoelectrons.

5.2 Monte Carlo Results

A Monte Carlo was constructed to model events of 120 – 240 photoelectrons by taking the ratio of two normally distributed, uncorrelated, random variables with mean and sigma given by equations (5.4) and (5.9). The distribution of the ratio of these two variables is shown in Figure 5.1. The Hinkley function and Monte Carlo are seen to be in good agreement.

By transforming the Monte Carlo events shown in Figure 5.1 to values of F_{Prompt} by equation (5.1), we produce the distribution in F_{Prompt}, shown in Figure 5.5.

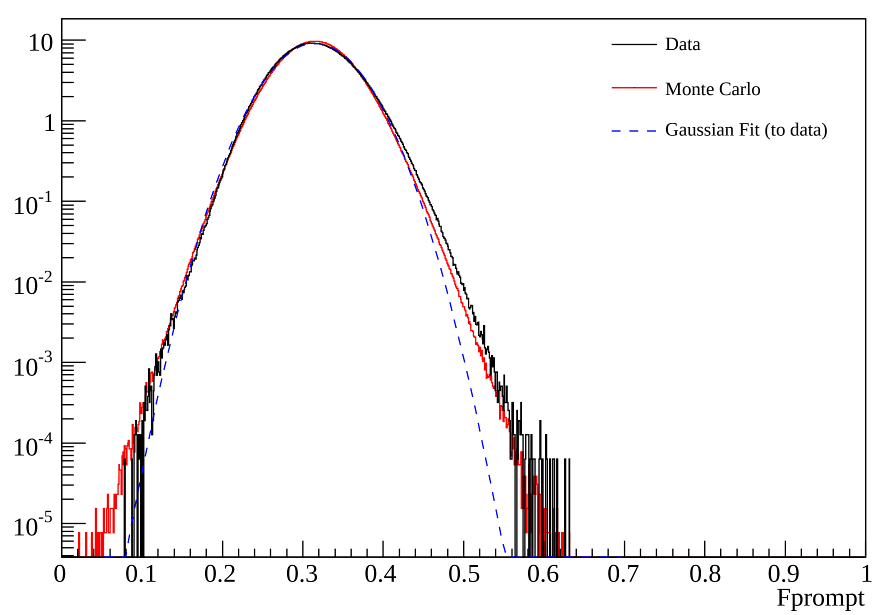

Figure 5.5: F_{Prompt} distribution for events of 120-240 photoelectrons

For comparison, a Gaussian function was fitted to the data. Note the increased width of the measured F_{Prompt} tail. The Monte Carlo distribution is shown to be in good agreement with the measured population of F_{Prompt}. The Monte Carlo shown here has been weighted to correct for energy dependence, to be described in section 5.4.

5.3 Prediction of Pulse Shape Discrimination

In stating the achievable discrimination level, we define a new parameter, P_{Leak}, as the probability of an event to leak above a value of F_{Prompt}, given by,

$$\mathrm{P}_{\mathrm{Leakage}}\left(F_{\mathrm{Prompt}} > r_n\right) = \frac{\int_{x=0}^{r_n} f\left(x\right)}{\int_{x=0}^{1} f\left(x\right)} \tag{5.10}$$

where f(x) is the distribution of F_{Prompt} events, now shown to be analytically given by equation (5.2), and r_n is obtained by transforming F_{Prompt} by equation (5.1),

$$\begin{aligned} F_{\mathrm{Prompt}} &= \frac{1}{1+r_{\mathrm{n}}} \\ \therefore r_{\mathrm{n}} &= \frac{1}{F_{\mathrm{Prompt}}} - 1 \end{aligned} \tag{5.11}$$

This probability is computed over the range of F_{Prompt}, for both data and the analytical function. The cumulative distribution function is shown in Figure 5.6.

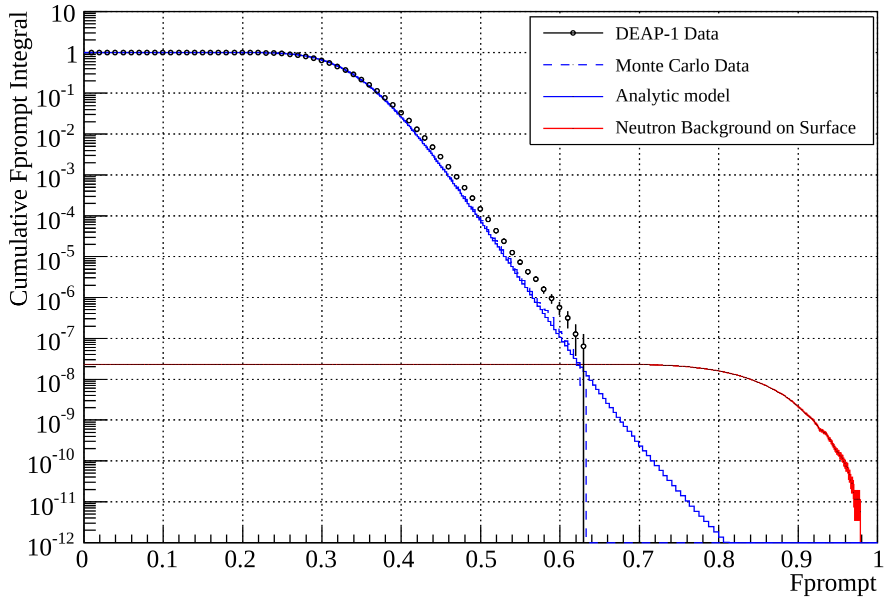

Figure 5.6: Monte Carlo and analytical prediction of discrimination.

In Figure 5.6 we see a very good agreement between the data, Monte Carlo and the analytical model.

For a population of 15.8 million correctly identified gamma events, we expect a discrimination of better than $1/(15.8 \times 10^6)$. The achieved discrimination here is found to be 6.3×10^{-8}.

To estimate the limit of the discrimination on surface due to background, we scale the Am-Be PSD curve by the expected rate of coincidence events in the energy region of interest. The annulus was only used to tag Na-22 gammas so we take into account the annulus trigger rate and window,

$$\begin{aligned}\frac{R_n}{R_\gamma} &= \frac{\text{high } \mathrm{F}_{\mathrm{Prompt}}\text{event rate}_{120\text{-}240\mathrm{PE}} \times \text{annulus trigger rate} \times \text{coincidence window}}{\text{event rate}_{120\text{-}240\mathrm{PE}}} \\ &= \frac{7 \text{ mHz} \times 2\times1000 \text{ Hz} \times 30 \text{ ns}}{18 \text{ mHz}} \\ &= 2.3\times10^{-8}\end{aligned} \tag{5.12}$$

The rate of high F_{Prompt} events in the energy region of interest is due to local neutron backgrounds and is expected to be reduced when operating underground in SNOLAB (see section 2.2.2.3. As the calibration set increases toward this limit we begin to see random coincidences with background events, hence the detector was moved underground once this limit was reached.

5.4 Energy Dependence

From the total energy spectrum we see a dependence of the number of events on the total number of photoelectrons. The spectrum over the energy scales of interest is shown in Figure 5.7.

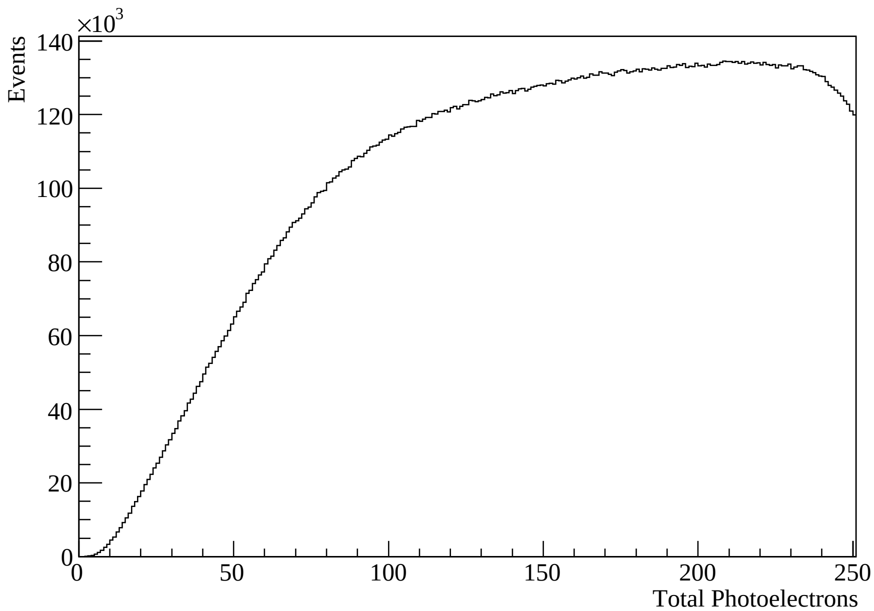

Figure 5.7: Total energy spectrum for events of up to 250 pe (0 - 89keV)

The spectrum varies by only a few percent for events of 120 – 240 photoelectrons, though is heavily dependent at lower energies. This is partially due to a large fraction of low energy events not passing the data cleaning cuts.

In order to calculate the cumulative F_{Prompt} distribution for an energy range of interest, we integrate over F_{Prompt} at regular intervals of a few photoelectrons wide, weighting each integral by the number of events, and average for the final distribution.

5.5 Model Applied to Lower Energy Scales

To adequately test the PSD model we apply it to events of lower energy, of 60 – 120 total photoelectrons. Given a light yield of 2.8 photoelectrons per keV, this scale is equivalent to 21 – 43 keV of energy, the energy scale of interest for a WIMP sensitive search.

Using the equations for the prompt and late parameters, equations (5.4) and (5.9), the F_{Prompt} population can be obtained from Monte Carlo simulation, shown in Figure 5.8.

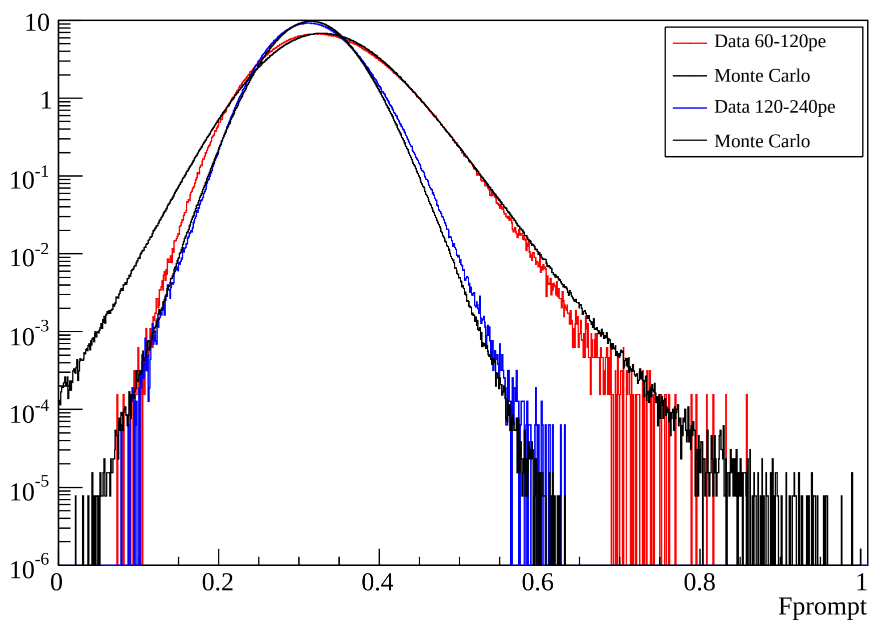

Figure 5.8: F_{Prompt} population at different energy scales

From the Monte Carlo, we see the parameters can be scaled to adequately represent the data at lower energy. The distribution is wider due to the increased uncertainty on F_{Prompt}

from the decrease in the total number of photoelectrons. It was shown in Figure 5.4 the uncertainty in the prompt and late components of the signal are dominated by statistical uncertainty. Given the singlet to triplet ratio in argon, a large decrease in total light would begin to decrease the resolution of the F_{Prompt} parameter, as indicated previously for electronic recoil in Figure 5.2.

The discrimination can then be determined by applying the parameters to the Hinkley equation, shown in Figure 5.9.

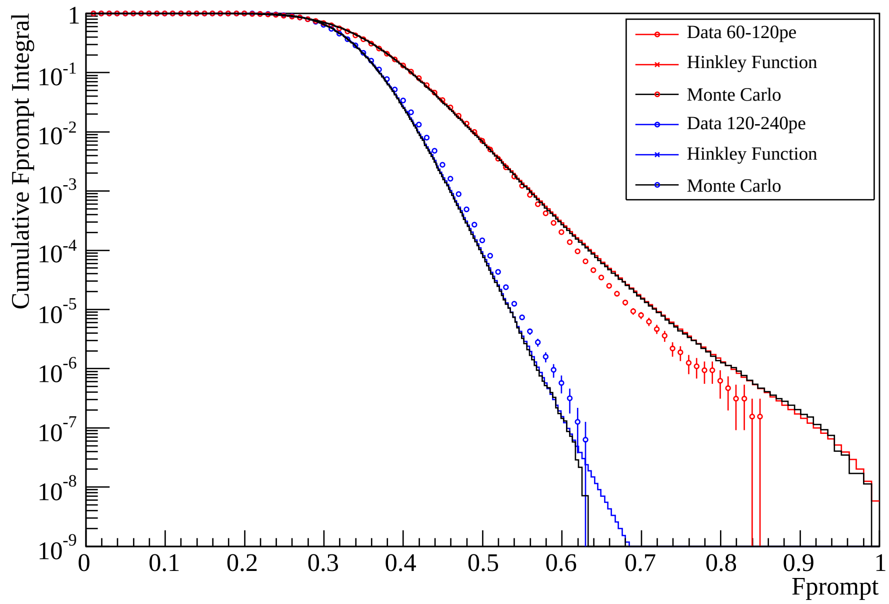

Figure 5.9: Statistical model for PSD over various energies

5.6 Effect of Noise on PSD

To predict further improvement to the detector, we can use parameters with reduced noise components to model the achievable discrimination. Improvements in the noise components, the late electrical component in particular, are believed possible by enhancement of the electronics, acquisition system and processing of events. In Figure 5.10 we show the limit of removing the noise components.

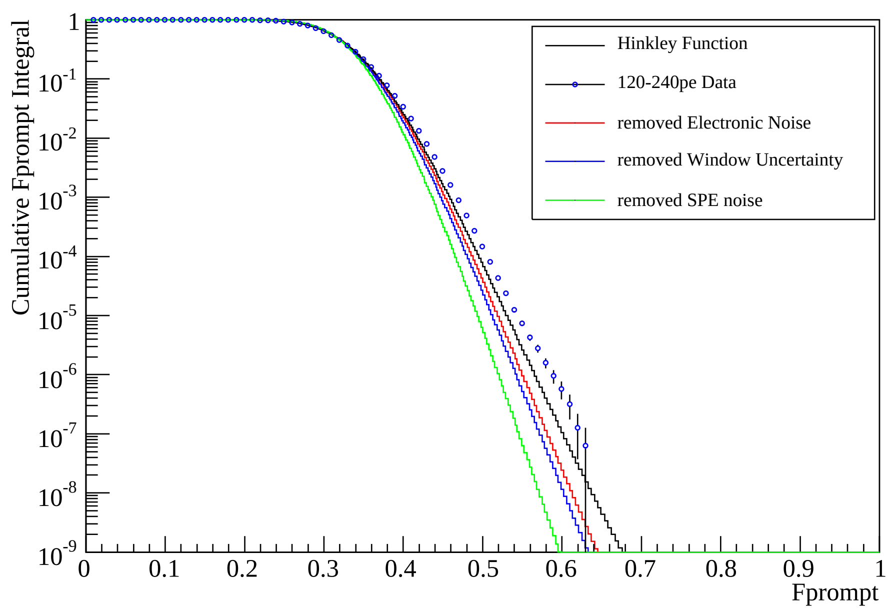

Figure 5.10: Predicted PSD with reduced components of noise

5.7 Systematic Effects of Noise on PSD

The noise parameters for the statistical model were adjusted to observe the effect of a systematic shift of each component. The effect on the discrimination is shown in Figure 5.11 for a ±10% variation in the number of total photoelectrons per event. Shown in Figure 5.12 are the effects due to variations in the electrical noise, window noise, SPE calibration and Fano factor. The effect of taking all these shifts into account is shown in Figure 5.13.

The most significant effects are due to shifts in energy, the electrical noise and the Fano factor. Some uncertainty in the energy is present, due to the uncertainty in the measured light yield, measured for the Ba-133 81 keV peak (section 4.3.1) to be ±7% and, due to the uncertainty in the SPE calibration. The electrical noise is also of concern as discussed in section 4.5.

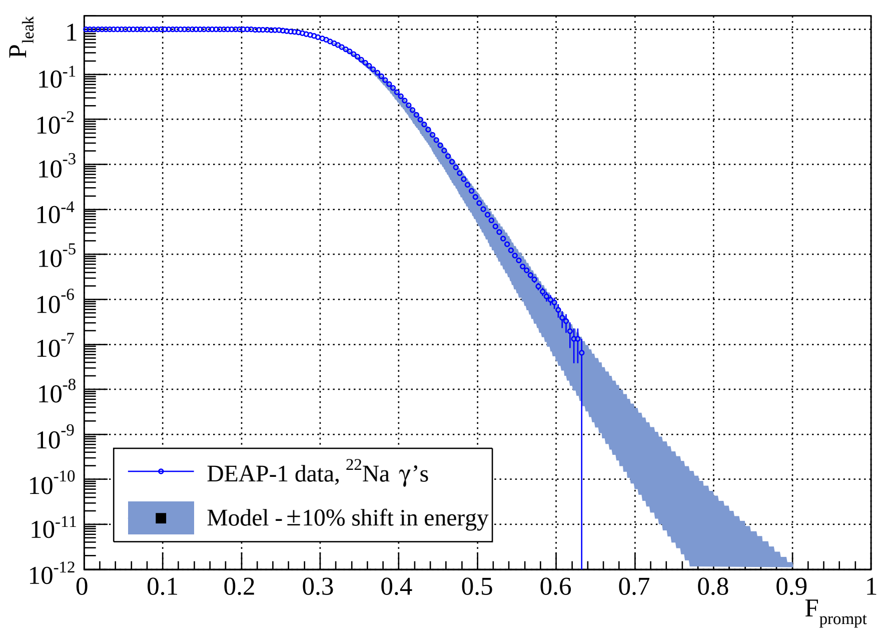

Figure 5.11: Effect of ±10% uncertainty in total photoelectrons

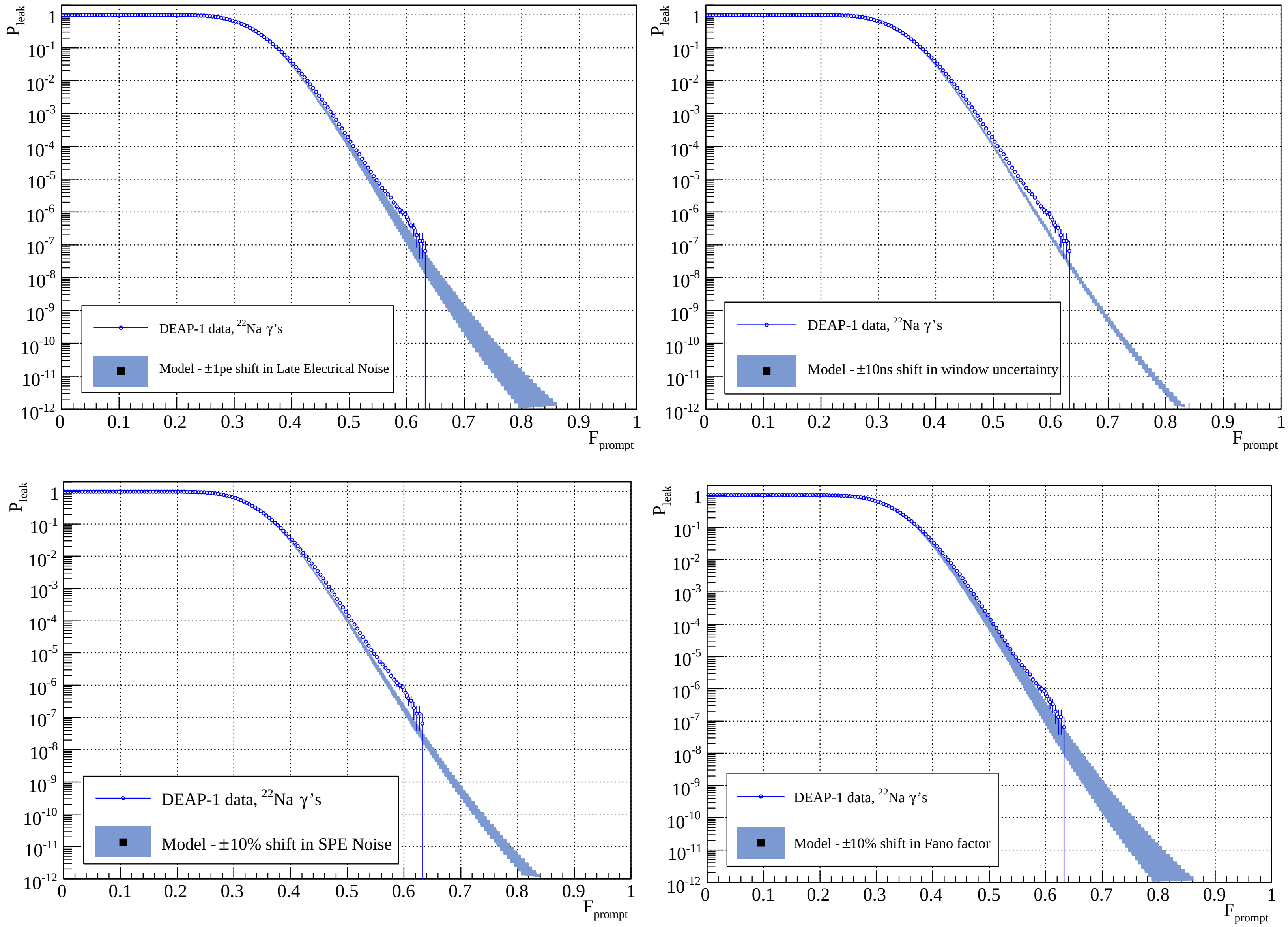

Figure 5.12: Effect on PSD from the systematic shifts

Late electrical noise (top left), window noise (top right), SPE calibration (bottom left) and the Fano factor (bottom right).

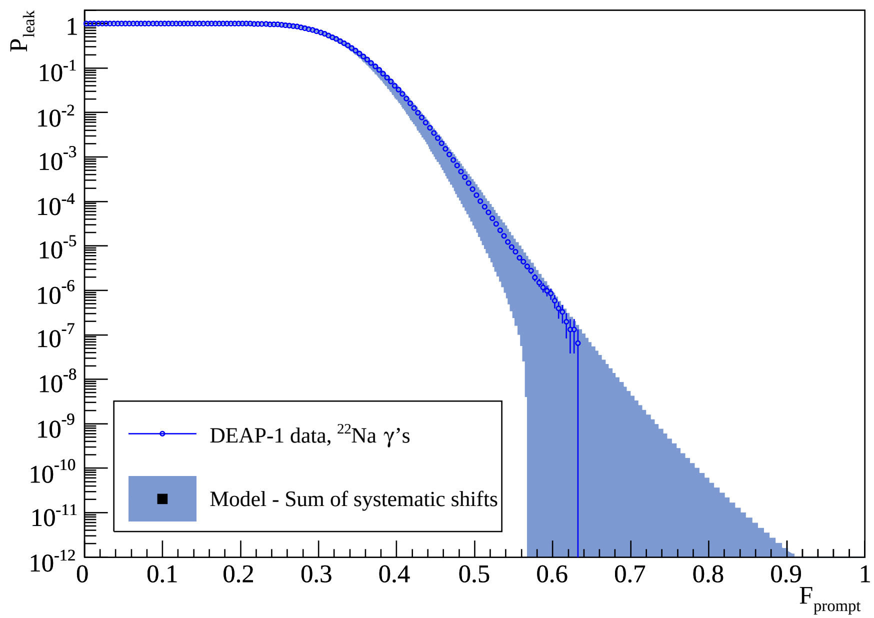

Figure 5.13: Sum of the studied systematic shifts

Chapter 6

Conclusions

6.1 Operation and Stability of Detector

The DEAP-1 detector was constructed and operated, on surface at Queen's with a target mass of 7 kg of liquid argon. The routine energy calibration proved the detector to be stable over the 2 month operational time. The light yield was measured to be 2.8 photoelectrons per keV.

6.2 Estimate of Achievable PSD

Over the 2 month operation of the detector on surface, a population of calibrated gamma events were collected to demonstrate discrimination at the level of 6.3×10^{-8}. This is more than sufficient to discriminate the internal background presented by argon-39.

In modelling the scintillation process, we have developed an analytical model, and tested it by Monte Carlo, that can accurately predict the measured data, as shown in Figure 6.1. The model parameters are dependent on a thorough understanding of the detector, namely the components of noise. By accurately measuring the detector characteristics a precise prediction of the achievable pulse shape discrimination can be made. The variation due to a 10% shift in energy is shown in Figure 6.1.

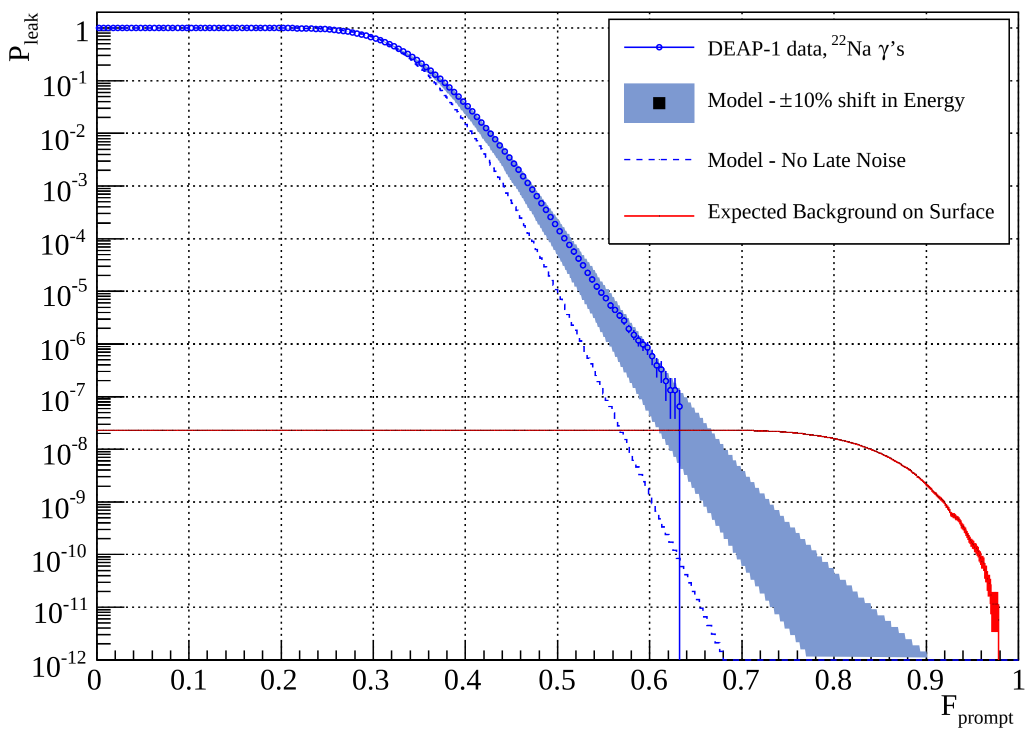

Figure 6.1: Achieved discrimination, MC and analytical prediction and surface background

The components of the noise were described in section 5.1, many of which can be reduced by further optimization and tuning of the detector, to the level desired by DEAP-3. An improvement in the discrimination by three orders of magnitude is desired for DEAP-3. The achievable discrimination of the detector with a reduction in the late noise, as predicted by the current model, is shown in Figure 6.1.

Through measurements of the background on surface we expect the achievable PSD on surface to be 2×10^{-8} due to neutron background, shown in Figure 6.1. The detector has been moved to SNOLAB for operation underground. In the underground operation of the detector we expect a decrease in background due to the reduced spallation rate. A reduced rate has been observed from initial measurements of the background underground. Further reduction in background is possible by reducing the radon contamination of the inner detector surfaces. The cleaning and re-coating of the detector in a nitrogen purged environment is currently underway to achieve this. The efficiency of the collection of calibration events could be increased by modifying the data acquisition and electronics. This will also aid the further demonstration of the achievable pulse shape discrimination.

6.3 Sensitivity to Dark Matter

In Figure 6.2 we present the expected WIMP sensitivity based on an active mass of 6.1 kg and 1 year of operation in SNOLAB.

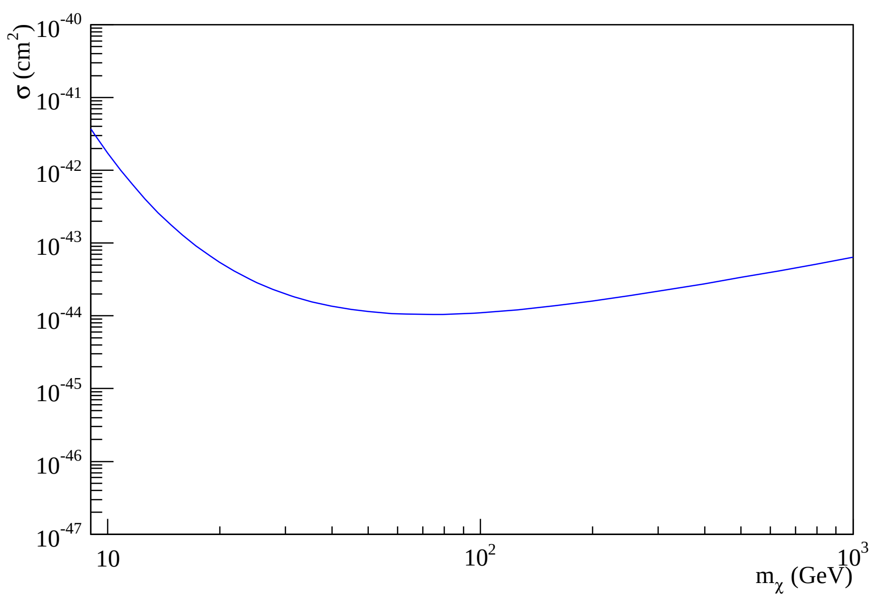

Figure 6.2: Dark matter limit for 6.1kg argon in 1 year of operation

Bibliography

[1] Freedman et al, Final Results from the Hubble Space Telescope Key Project to Measure the Hubble Constant arXiv:astro-ph/0012376v1, 18 Dec 2000.

[2] E. Komatsu, et.al, WMAP Collaboration. Five-Year Wilkinson Microwave Anisotropy Probe (WMAP) Observations: Cosmological Interpretation. arXiv: astro-ph/0803.0547v1, 4 Mar 2008

[3] F. Zwicky, Helv. Phys. Acta 6 (1933) 110.

[4] S. Van Den Bergh. The Early History of Dark Matter. The Astronomical Society of the Pacific, 111:657È660, 1999 June.

[5] Miralda-Escude, J. The mass distibution in clusters of galaxies from weak and strong lensing. arXiv: astro-ph/9509077, Sep 1995.

[6] M. Bradac et al, A direct empirical proof of the existence of dark matter. arXiv: astro-ph/0608407, 19 Aug 2006

[7] G. Jungman, M. Kamionkowski, K. Griest. Supersymmetric Dark Matter. Phys. Rep. 267, 195 (1996).

[8] M. Dragowsky CDMS Collaboration. A Search for WIMPs with the First Five-Tower Data from CDMS. arXiv: astro-ph/0802.3530v1, 24 Feb 2008

[9] E. Aprile. XENON Collaboration. First Results from the XENON10 Dark Matter Experiment at the Gran Sasso National Laboratory. arXiv: astro-ph/0706.0039v2, 3 Dec 2007

[10] The SNO Collaboration. "Measurement of the Total Active 8B Solar Neutrino Flux at the Sudbury Neutrino Observatory with Enhanced Neutral Current Sensitivity". Phys. Rev. Lett. volume 92, 181301 (2004).

[11] The SNO Collaboration. "Direct Evidence for Neutrino Flavor Tranformation from Neutral-Current Interactions in the Sudbury Neutrino Observatory". Phys. Rev. Lett. volume 89, No. 1, 011301 (2002).

[12] The Super-Kamiokande Collaboration. Evidence for oscillation of atmospheric neutrinos. Phys. Rev. Lett. 81 (1998) 1562-1567

[13] KamLAND Collaboration. First Results from KamLAND: Evidence for Reactor Anti-Neutrino Disappearance. arXiv:hep-ex/0212021v1. 9 Dec 2002

[14] A. Corsetti, P. Nath. SUSY Dark Matter. arXiv:hep-ph/0005234v1 23 May 2000

[15] T. Schutt. A Dark Matter detector based on the Simultaneous Measurements of Phonons and Ionization at 20mK. Ph.D thesis U.C. Berkeley. 1993.

[16] Boulay, M. & Hime, A. Technique for direct detection of weakly interacting massive particles using scintillation time discrimination in liquid argon. Journal of Astroparticle Physics 25 (2006) 179–182.

[17] SNOLAB. INCO Creighton Mine #9 Ontario, Canada. www.SNOLAB.ca

[18] M. Barnabe-Heider et al. PICASSO Collaboration. Response of superheated droplet detectors of the picasso dark matter search experiment. Aug 2005. Nucl. Instrum. Meth. A555:184-204, 2005 (arXiv: physics/0508098)

[19] M. Barnabe-Heider et al. PICASSO Collaboration. Improved spin dependent limits from the PICASSO dark matter search experiment. Feb 2005 Phys.Lett. B624:186-194, 2005 (arXiv:hep-ex/0502028)

[20] M.G. Boulay, A. Hime, J. Lidgard. Design Constraints for a WIMP Dark Matter and pp Solar Neutrino Liquid Neon Scintillation Detector. arXiv:nucl-ex/0410025v1. 18 Oct 2004

[21] D. McKinsey, A. Hime. et al. Scintillation time dependence and pulse shape discrimination in liquid argon. arXiv: nucl-ex/0801.1531v1,10 Jan 2008

[22] J. A. Nikkel, R. Hasty, W. H. Lippincott, and D. N. McKinsey. Scintillation of liquid neon from electronic and nuclear recoils. 4 Dec 2006 arXiv:astro-ph/0612108v1.

[23] D0 Collaboration. The Upgraded D0 Detector. arXiv:physics/0507191 (Submitted to Nucl. Instrum. Methods A).

[24] Rubbia, C. (WARP collaboration). WARP liquid argon detector for dark matter survey. arXiv:astro-ph/0405342v1, 18 May 2004

[25] C. Amsler. Luminescence quenching of the triplet excimer state by air traces in gaseous argon. arXiv:0708.2621v1, 20 Aug 2007

[26] R. Michniaka, R. Alleaume, D. McKinsey, J. Doyle. Alpha and beta particle induced scintillations in liquid and solid neon. Nuclear Instruments and Methods in Physics Research A 482 (2002) 387–394.

[27] M. Boulay, DEAP-3 NSERC Proposal 200612, Queen's University, 2007

[28] T. Doke, K. Masuda, E. Shibamura. Estimation of absolute photon yields in liquid argon and xenon for relativistic (1MeV) electrons. Nuclear Instruments and Methods in Physics Research A291 (1990) 617-620.

[29] A. Hitachi, T. Takahashi. Effect of ionization density on the time dependence of luminescence from liquid argon and xenon. Phys. Rev. B Vol 27 no 9 (1983) 5279

[30] A. Hitachi, T. Doke, A. Mozumder. Luminescence quenching in Liquid Argon under charged-particle impact: Relative scintillation yield at different linear energy transfers. Phys. Rev. B Vol 46 no 18 (1992) 11463

[31] E. Aprile, K. L. Giboni, P. Majewski, K. Ni, M. Yamashita, R. Hasty, A. Manzur, and D. N. McKinsey. Scintillation response of liquid xenon to low energy nuclear recoils. Phys. Rev. D 72, 072006 (2005)

[32] SAES Getters. Monotorr PS4-MT3/MT15 Heated Getter Purifiers. www.saespuregas.com

[33] M. Boulay, DEAP-3 NSERC Proposal 327126, Queen's University.

[34] J. W. Gallagher, C. E. Brion, J. A. R. Samson and P. W. Langhoff. Absolute cross-sections for Molecular Photoabsorbtion, Partial Photoionization, and Ionic Photofragmentatino Processes. J. Phys. Chem. Ref. Data, Vol 17, No. 1, 1988.

[35] H. H. Loosli, H. Oeschger, Detection of ^{39}Ar in Atmospheric Argon. Earth and Planetary Science Letters, (1968) 191.

[36] H. H. Loosli, A Dating Method with ^{39}Ar. Earth and Planetary Science Letters, 63, (1983) 51.

[37] L. Pandola (WARP collaboration). Measurement of the specific activity of Ar-39 in natural argon. arXiv:astro-ph/0603131v2, 10 Jan 2007

[38] C. Galbiati, R. Purtschert et. al. Discovery of underground argon with low level of radioactive ^{39}Ar and possible applications to WIMP dark matter detectors. arXiv:0712.0381v1, 3 Dec 2007

[39] M. G Stabin, L. C.Q.P. da Luz. Decay Data for Internal and External Dose Assessment. Health Phys. 83(4):471-475, 2002. Found on the web at the RAdiation Dose Assessment Resource (RADAR) www.doseinfo-radar.com

[40] SNO Collaboration, SNO Annex.

[41] M. Boulay. Neutron and Gamma ray backgrounds in DEAP-1 (preliminary). September 2006.

[42] National Nuclear Data Centre, Brookhaven National Laboratory. www.nndc.bnl.gov.

[43] D.-M. Mei, A. Hime. Muon-Induced Background Study for Underground Laboratories

[44] Thermodynamics Research Center, NIST Boulder Laboratories, "Thermodynamics Source Database" in NIST Chemistry WebBook, (http://webbook.nist.govtm

[45] MDC Catalogue – Del-Seal CF Reducing Tees – 8” x4-5/8” Tee - UHV Series Part Number 404056. www.mdcvacuum.com

[46] MDC Catalogue – Viewports & Glass Components – Viewports Zero Profile 7056 Glass - UHV Series Part Number – 450008. www.mdcvacuum.com

[47] M. Boulay, Design & Thermodynamic studies for DEAP-0, Los Alamos National Laboratory, 2005.

[48] Pfeiffer Vacuum Turbomolecular pumping stations TSH 071 E, DN 63 ISO-K with TPS 100. www.pfeiffer-vacuum.com

[49] TPB source

[50] D. McKinsey, S. Lamoreaux. Fluorescence efficiencies of thin scintillating films in the extreme ultraviolet spectral region. Nuclear Instruments and Methods in Physics Research B 132 (1997) 351-358

[51] Saint Gobain Organic Scintillators. BC-620 Reflector Paint for Plastic Scintillators www.detectors.saint-gobain.com (see Library / Data Sheets / BC-620)

[52] James A. Nikkel, W. Hugh Lippincott, and Daniel N. McKinsey. Demonstration of photomultiplier tube operation at 29 K. arXiv:astro-ph/0702202v1 7 Feb 2007

[53] Electron Tubes 9390 5” photomultiplier tube. www.electrontubes.com/pdf/9390B.pdf

[54] P. Pasuthip, To be published. Master’s Thesis, Queen’s University.

[55] Duderstadt & Hamilton. Nuclear Reactor Physics. John Wiley & Sons. 1976.

[56] LeCroy WavePro Oscilloscope. www.lecroy.com

[57] Chandler, H. H., Bowen, R. L., and Paffenbarger, G. C. Physical properties of a radiopaque denture base material. J. Biomed. Mater. Res., 5(4):335-357, 1971.

[58] H. Vega-Carrillo, E, Manzanares-Acuna, A. Becerra-Ferreiroa, A. Carrillo-Nunez. Neutron and gamma-ray spectra of 239PuBe and 241AmBe. Applied Radiation and Isotopes 57 (2002) 167–170.

[59] Heimbach. C, NIST calibration of a neutron spectrometer ROSPEC. Journal of Research of NIST v111, number 6, Dec 2006.

[60] S. Croft, The use of neutron intensity calibrated 9Be(α, n) sources as 4438 keV gamma-ray reference standards. Nucl. Instr. Meth. A281 (1989) 103.

[61] DEAP-1 Queen's University Surface run database (2007) used in analysis:

Sodium-22 PSD data run numbers: 411, 412, 413, 414, 415, 416, 420, 421, 422, 427, 428, 429, 430, 490, 491, 492, 493, 494, 496, 497, 498, 521,522, 523, 525, 528, 529, 532, 533.

Sodium-22 Energy calibration run numbers: 312, 323, 363, 419, 426, 445,473, 495, 501, 513, 518, 524, 527, 531.

Am-Be Neutron run numbers: 316.

Background measurement run numbers: 436, 437, 438, 448, 476, 478, 479, 480, 482, 486, 487, 488, 489.

[62] L.P. Ekström and R.B. Firestone, WWW Table of Radioactive Isotopes, database version 2/28/99 http://ie.lbl.gov/toi/index.htm

[63] D. V. Hinkley. On the Ratio of Two Correlated Normal Random Variables. Biometrika, Vol. 56, No. 3. (Dec., 1969), pp. 635-639.